Facilitating Realistic and Efficient Applications of Ab Initio Electronic Dynamics for Polyatomic Systems

Phu D. Nguyen

A dissertation
submitted in partial fulfillment of the
requirements for the degree of

Doctor of Philosophy

University of Washington

2016

Reading Committee:
Xiaosong Li, Chair
Lutz Maibaum
David Masiello

Program Authorized to Offer Degree:
Chemistry

Facilitating Realistic and Efficient Applications of Ab Initio Electronic Dynamics for Polyatomic Systems

Abstract

Phu D. Nguyen

Chair of the Supervisory Committee:

Professor Xiaosong Li

Department of Chemistry

Tremendously useful insights for the design and development of nano-scale systems, e.g. photovoltaics devices, can be gained from studying molecular process and reactions using *ab initio* electronic dynamics, i.e. applying methods derived from the time-dependent Schoödinger equation (TDSE) to describe movement of electrons. This work will examine how we can optimize and adapt one such method, the time-dependent density functional theory (TD-DFT) formalism, which has been proven to be efficient and relatively accurate, to complex and large molecules such as polymeric structures. After the benefits and shortcomings of TD-DFT has be thoroughly considered, we will present attempts – with varying degrees of success, at augmenting and mitigating the deficiency of TD-DFT.

Contents

Listing of figures

To God and His glory.

To whoever might find my dissertation interesting and/or useful.

Acknowledgments

I cannot overstate how grateful I am for the following individuals:

My advisor, Prof. Xiaosong Li, who has lavishly provided constant and dependable support, guidance, and encouragement throughout my study and beyond.

Current and former group mates: Dr. Feizhi Ding, Erica Chong, Dr. Sean A. Fischer, Bo Peng, Patrick Lestrange, Dr. Wenkel Liang – thank you all for your support, advice, and patience.

And finally, my parents, who have always been there for me and be patient with me. Thank you for always encouraging me to embark on adventures, especially this one.

Einstein's theory of relativity does a fantastic job for explaining big things. Quantum mechanics is fantastic for the other end of the spectrum – for small things.

Brian Greene

1 Introduction

Similar to other physical sciences, chemistry is the study of matter and its properties (as well as interactions with other matter and with energy – but we'll get to that later). However, chemistry tends to focus more on reactions and processes that involve the electrons as most, if not all, of a material's properties depend heavily on its electronic structure. Unfortunately, the elusive nature of the electrons often prevents the direct and/or reliable measurement of such properties. Therefore, in principle, all properties of a given material can be determined **IF** somehow a chemist know for the exact electronic structure of such material. Not only could static properties be readily calculated, simulating how they change under certain condition is as simple as iteratively updating the electronic structure and configuration of the nuclei.

In 1926, with his celebrated paper,[2] Edwin Schrödinger not only introduced the wave mechanics of electrons but also the entire field of *ab initio* electronic structure theory. In a sense, decades of research in the field of quantum mechanics since then have been to find approximate solutions of the non-relativistic time-dependent Schrödinger equation (TDSE) for N electrons

and M nuclei:

$$\hat{H}\,|\Psi\rangle = E\,|\Psi\rangle \tag{1.1}$$

with

$$\hat{H} = \hat{H}_{\text{nucl}} + \hat{H}_{\text{elec}} \tag{1.2}$$

$$\hat{H}_{\text{nucl}} = -\sum_{A=1}^{M} \frac{1}{2M_A}\nabla_A^2 + \sum_{A=1}^{M}\sum_{B>A}^{M} \frac{Z_A Z_B}{R_{AB}} \tag{1.3}$$

$$\hat{H}_{\text{elec}} = -\sum_{i-1}^{N} \frac{1}{2}\nabla_i^2 - \sum_{i=1}^{N}\sum_{A=1}^{M} \frac{Z_A}{r_{iA}} + \sum_{i=1}^{N}\sum_{j>i}^{N} \frac{1}{r_{ij}} \tag{1.4}$$

where atomic units have been used.

All chemical systems, regardless of sizes and types, always undergo some sort of process or reaction, and almost every one these processes is driven by movement of the electrons. Obtaining an accurate static electronic structure for a system is already challenging task, and much can be learned from such static "snapshots," we can never probe the immensely interesting non-equilibrium dynamics underlying these processes.

Throughout my graduate study career, I have always been interested in using such approximations of the TDSE such as time-dependent Hartreee-Fock (TDHF) or time-dependent density-functional theory (TDDFT) to study experimentally relevant molecular systems, e.g. semiconductor nanocrystals, organovoltaic polymers, peptides, etc. Computationally, such interests mean dealing with relatively large molecules (20 or more atoms), going beyond the first-row elements, and working with external driving forces such as photoexcitation and solvent environments. Thus, a major area of research in my study was efficient and realistic first-principles modeling of molecular systems.

This work will serve as journal documenting the progress I have made during my research career. The successes have become published papers,[3,4,5,6] while failures are dearly treasured as invaluable learning opportunities.

In Chapter 2, I will explain in reasonable details the principles and theories I have used, including Hartree-Fock (HF) approximation, density functional theory (DFT), their time-dependent equivalence TDHF and TDDFT. Chapter 3 should give readers a glimpse at my

typical research workflow: starting from experimental data, how I would deconstruct the task at hands into computationally feasible simulations, then combine existing methods and techniques into as realistic as possible a model for molecular system in questions. Chapter 3 also demonstrates the type of molecular systems I often work with as well as pays due attention to resonance photoelectric spectroscopy, a nascent yet powerful experimental technique. Since most of my calculations are done in the DFT framework, Chapter 4 will address what is regarded as the crux of DFT: choosing the exchange functionals. The experiment described in Chapter 3 is an extension of the veteran X-ray absorption spectroscopy (XAS), and in Chapter 4 I will investigate how well existing DFT functionals can reproduce experimental XAS spectra. Chapter 5 will present the highlights of my research on the next step in solving a time-dependent problem: a proposed numerical solution to the time-evolution with a time-dependent perturbation component from the environment. And last but not least, Chapter 6 presents my preliminary efforts in accelerating the propagation of the TDDFT equation using the Chebyshev polynomial approach.

Protons give an atom its identity, electrons its personality.

Bill Bryson

2

Electronic Structure of Molecules: the Basics

Similar to other physical sciences, chemistry is the study of matter and its properties (as well as interactions with other matter and with energy – but we'll get to that later). However, chemistry tends to focus more on reactions and processes that involve the electrons as most, if not all, of a material's properties depend heavily on its electronic structure. Unfortunately, the elusive nature of the electrons often prevents the direct and/or reliable measurement of such properties. Therefore, in principle, all properties of a given material can be determined *if somehow* a chemist know the exact electronic structure of such material. Not only could static properties be readily calculated, simulating how they change under certain condition is as simple as iteratively updating the electronic structure and configuration of the nuclei. However, solving for the exact electronic structure for a given system is still a primary crux of quantum chemistry.

In general, the terms ”electronic structure” and ”electron density” both refers to a set of probability distribution functions which provide the probability of finding an electron at a certain point in time and space.

Since the nuclei are heavier than electrons by several orders of magnitude, their movement consequently happen on a much slower timescale ; thus one can consider the electrons in a molecule to be moving in the field of fixed nuclei. The nuclei structure can then be depicted as point charges that are either static or have well defined trajectories. Within this approximation, the kinetic energy term, the first term of $\hat{H}$, is ignored while the nuclear repulsion, the second term, is considered constant. This is the Born-Oppenheimer approximation. The remaining task is then dealing with the electronic Hamiltonian.

The first two terms of $\hat{H}_{\text{elec}}$, kinetic energy and nuclear-electron attraction, are sums of single-electron operators and will be collectively denoted as $\hat{h}_1$, while the last term, electron-electron interaction, acts on pairs of electrons, hence denoted as $\hat{h}_2$. From this point forward:

$$\hat{H} \approx \hat{H}_{\text{elec}} = -\sum_{i-1}^{N} \frac{1}{2}\nabla_i^2 - \sum_{i=1}^{N}\sum_{A=1}^{M} \frac{Z_A}{r_{iA}} + \sum_{i=1}^{N}\sum_{j>i}^{N} \frac{1}{r_{ij}} \tag{2.1}$$

$$= \sum_i \hat{h}_1(\vec{x}_i) + \sum_i \sum_{j>i} \hat{h}_2(\vec{x}_i, \vec{x}_j) \tag{2.2}$$

unless stated otherwise. $\vec{x}_i$ is now a generalized coordinate including both spatial and spin degrees of freedoms.

2.1 The Hartree-Fock (HF) Approximation

The HF method is a variational, wave-functioned based, many-body technique in a single-particle picture, i.e. each electron occupies a single-particle orbital and feels the presence of other electrons indirectly via an effective potential. Even though the HF method is no longer at the cutting-edge of electronic structure theory and seldom used, its principles always hold true and serves as the backbone for higher levels of theory.

HF suggests that a good starting ansatz for the variational wave function Ψ is the direct product of single-electron orbitals φ_i:

$$\Psi(\vec{x}_1, \ldots, \vec{x}_N) = \varphi_m(\vec{x}_1)\varphi_n(\vec{x}_2)\cdots\varphi_N(\vec{x}_N) \tag{2.3}$$

As the orbitals φ_i's are wave functions themselves, they must be orthonormal, i.e

$$\int_{-\infty}^{\infty} \varphi_i^* \varphi_j = \langle \varphi_i | \varphi_j \rangle = \langle i | j \rangle = \delta_{ij} \tag{2.4}$$

This is known as the Hartree approximation. Because of the Pauli exclusion principle, the posited many-electron wave function must also satisfy the anti-symmetry principle, i.e. changing sign under odd permutations of coordinate variable $\vec{x}_i$:

$$\Psi(\vec{x}_1, \ldots, \vec{x}_m, \ldots, \vec{x}_n, \ldots, \vec{x}_N) = -\Psi(\vec{x}_1, \ldots, \vec{x}_n, \ldots, \vec{x}_m, \ldots, \vec{x}_N) \tag{2.5}$$

Dr. John Slater[7] came up with a better ansatz using a determinant. For a system with N electrons, the wave function is taken to be:

$$\begin{aligned} \Psi(\vec{x}_1, \ldots, \vec{x}_N) &\approx \frac{1}{\sqrt{N!}} \begin{vmatrix} \varphi_1(\vec{x}_1) & \varphi_2(\vec{x}_1) & \cdots & \varphi_N(\vec{x}_1) \\ \varphi_1(\vec{x}_2) & \varphi_2(\vec{x}_2) & \cdots & \varphi_N(\vec{x}_2) \\ \vdots & \vdots & \ddots & \vdots \\ \varphi_1(\vec{x}_N) & \varphi_2(\vec{x}_N) & \cdots & \varphi_N(\vec{x}_N) \end{vmatrix} \\ &= \frac{1}{\sqrt{N!}} \sum_i^{N!} (-1)^{p_i} \hat{P}_i \{ \varphi_m(\vec{x}_1) \varphi_n(\vec{x}_2) \cdots \varphi_z(\vec{x}_N) \} \\ &= |\varphi_m \varphi_n \cdots \varphi_z\rangle \\ &= |m\, n \cdots z\rangle \end{aligned} \tag{2.6, 2.7}$$

where the factor in the front ensures normalization. $\hat{P}_i$ is a operator that generate the i^{th} permutation of the electron labels $1, 2, \ldots, N$ and p_i is the number of interchanges required to obtain this permutation. Various shorthand notations for Slater determinant are introduced and will be used when appropriate.

According to the variational principle, the "best" orbital set would minimize the electronic energy:

$$\langle \Psi | \hat{H} | \Psi \rangle = \langle \Psi | \sum_n \hat{h}_1(\vec{x}_n) | \Psi \rangle + \langle \Psi | \sum_m \sum_{n>m} \hat{h}_2(\vec{x}_m, \vec{x}_n) | \Psi \rangle \tag{2.8}$$

First, we tackle the one-electron term. Because electrons are indistinguishable, the outcome of

$\hat{h}_1(\vec{x}_1)$ will be identical to $\hat{h}_1(\vec{x}_2)$, $\hat{h}_3(\vec{x}_N)$, etc; we can just arbitrarily choose the operator for electron 1 to work with and write the term as:

$$\begin{aligned}\langle\Psi|\sum_n^{N!}\hat{h}_1(\vec{x}_n)|\Psi\rangle &= \sum_n^{N!}\langle\Psi|\hat{h}_1(\vec{x}_1)|\Psi\rangle \\ &= \frac{N}{N!}\sum_i^{N!}\sum_j^{N!}\Big[(-1)^{p_i}(-1)^{p_j}\hat{P}_i\{\langle\varphi_m(\vec{x}_1)\varphi_n(\vec{x}_2)\cdots\varphi_N(\vec{x}_N)|\} \\ &\qquad \hat{h}_1(\vec{x}_1)\hat{P}_j\{|\varphi_m(\vec{x}_1)\varphi_n(\vec{x}_2)\cdots\varphi_N(\vec{x}_N)\rangle\}\Big] \qquad (2.9)\end{aligned}$$

There are 2 types of integrals in eq. (2.9):

$$\langle\varphi_m(\vec{x}_1)|\hat{h}_1(\vec{x}_1)|\varphi_n(\vec{x}_1)\rangle = \delta_{mn}\varepsilon_1 \qquad (2.10)$$

$$\langle\varphi_m(\vec{x}_i)|\varphi_n(\vec{x}_i)\rangle = \delta_{mn} \qquad (2.11)$$

Only when the electrons occupy the same spin orbitals in both permutations will we get a non-zero result for eq. (2.9), i.e. we only need to keep track of one permutation:

$$\begin{aligned}&\langle\Psi|\sum_i\hat{h}_1(\vec{x}_i)|\Psi\rangle \\ =&\frac{1}{(N-1)!}\sum_{i,j}^{N!}\hat{P}_i\{\langle\varphi_m(\vec{x}_1)\varphi_n(\vec{x}_2)\cdots\varphi_N(\vec{x}_N)|\}\hat{h}_1(\vec{x}_1)\hat{P}_i\{|\varphi_m(\vec{x}_1)\varphi_n(\vec{x}_2)\cdots\varphi_N(\vec{x}_N)\rangle\} \qquad (2.12)\end{aligned}$$

Electron 1 will occupy each orbital φ_i once, leaving $(N-1)!$ ways to arrange electrons $2, 3, \ldots, N$. Thus, among the $N!$ permutations inside the sum, there are N integrals as in eq. (2.10) and $(N-1)!$ occurrences of the integral in eq. (2.11), each of which integrates to 1. Equation (2.9) then becomes:

$$\begin{aligned}\langle\Psi|\sum_n\hat{h}_1(\vec{x}_n)|\Psi\rangle &= \frac{(N-1)!}{(N-1)!}\sum_m^N\langle\varphi_m(\vec{x}_1)|\hat{h}_1(\vec{x}_1)|\varphi_m(\vec{x}_1)\rangle \\ &= \sum_m^N\langle m|\hat{h}_1|m\rangle \qquad (2.13)\end{aligned}$$

Now we turn to the much, much more complicated two-electron term.

$$\sum_{m}^{N}\sum_{m>n}^{N}\langle\Psi|\hat{h}_2(\vec{x}_m,\vec{x}_n)|\Psi\rangle=\sum_{m}^{N}\sum_{m>n}^{N}\langle\Psi|r_{mn}^{-1}|\Psi\rangle \tag{2.14}$$

Similar to $\hat{h}_1$, each of the r_{mn}^{-1} term will give the same result for any pair of electrons, thus we can replace it with a single operator r_{12}^{-1} and multiply by the possible number of pairs of electrons:

$$\sum_{m}^{N}\sum_{m>n}^{N}\langle\Psi|r_{mn}^{-1}|\Psi\rangle=\binom{N}{2}\langle\Psi|r_{12}^{-1}|\Psi\rangle=\frac{N!}{2!(N-2)!}\langle\Psi|r_{12}^{-1}|\Psi\rangle=\frac{N(N-1)}{2}\langle\Psi|r_{12}^{-1}|\Psi\rangle \tag{2.15}$$

$$=\frac{N(N-1)}{2\cdot N!}\sum_{i}^{N!}\sum_{j}^{N!}\Big[(-1)^{p_i}(-1)^{p_j}\hat{P}_i\{\langle\varphi_m(\vec{x}_1)\varphi_n(\vec{x}_2)\cdots\varphi_z(\vec{x}_N)|\}\, r_{12}^{-1}\,\hat{P}_j\{|\varphi_m(\vec{x}_1)\varphi_n(\vec{x}_2)\cdots\varphi_z(\vec{x}_N)\rangle\}\Big] \tag{2.16}$$

r_{12}^{-1} involves both electrons 1 and 2 (e_1^- and e_2^-). If e_1^- and e_2^- occupy some arbitrary φ_k and φ_l orbitals in the bra, i.e:

$$\hat{P}_i\{\langle\varphi_m(\vec{x}_1)\varphi_n(\vec{x}_2)\cdots\varphi_z(\vec{x}_N)|\}=\langle\cdots\varphi_k(\vec{x}_1)\varphi_j(\vec{x}_2)\cdots|$$

We have two choices for the ket:

$$\hat{P}_j\{|\varphi_m(\vec{x}_1)\varphi_n(\vec{x}_2)\cdots\varphi_z(\vec{x}_N)\rangle\}=\begin{cases}|\cdots\varphi_k(\vec{x}_1)\varphi_l(\vec{x}_2)\cdots\rangle\\ |\cdots\varphi_l(\vec{x}_1)\varphi_k(\vec{x}_2)\cdots\rangle\end{cases}$$

Let $\hat{P}_{12}$ be an operator that interchanges the coordinates of e_1^- and e_2^-, i.e.:

$$\hat{P}_{12}\{|\cdots\varphi_k(\vec{x}_1)\varphi_l(\vec{x}_2)\cdots\rangle\}=|\cdots\varphi_k(\vec{x}_2)\varphi_l(\vec{x}_1)\cdots\rangle \tag{2.17}$$

Using the exchange operator notation, eq. (2.16) becomes:

$$\sum_{m}^{N}\sum_{m>n}^{N}\langle\Psi|r_{mn}^{-1}|\Psi\rangle = \frac{1}{2(N-2)!}\sum_{i}^{N!}\Big[\hat{P}_i\{\langle\varphi_m(\vec{x}_1)\varphi_n(\vec{x}_2)\cdots\varphi_z(\vec{x}_N)|\}\, r_{12}^{-1} \left(1-\hat{P}_{12}\right)\hat{P}_i\{|\varphi_m(\vec{x}_1)\varphi_n(\vec{x}_2)\cdots\varphi_z(\vec{x}_N)\rangle\}\Big] \tag{2.18}$$

where we have folded 2 choices of the ket into the $(1-\hat{P}_{12})$ factor. The negative sign comes from the antisymmetry nature of Slater determinant, i.e. $\hat{P}_i = -\hat{P}_{12}\hat{P}_i$ for a given i^{th} permutation. Similar to the one-electron case, the remaining electrons $3, 4, \ldots, N$ will have to occupy the same orbitals in the bra as in the ket; and there are $(N-2)!$ ways to arrange them, giving $(N-2)!$ matching $\langle\varphi_m|\varphi_m\rangle = 1$ terms. Equation (2.16) can then be greatly simplified:

$$\sum_{m}^{N}\sum_{m>n}^{N}\langle\Psi|r_{mn}^{-1}|\Psi\rangle = \frac{(N-2)!}{2(N-2)!}\sum_{m}^{N}\sum_{n\neq m}^{N}\langle\varphi_m(\vec{x}_1)\varphi_n(\vec{x}_2)|\, r_{12}^{-1}\left(1-\hat{P}_{12}\right)|\varphi_m(\vec{x}_1)\varphi_n(\vec{x}_2)\rangle \tag{2.19}$$

$$= \frac{1}{2}\sum_{m}^{N}\sum_{n\neq m}^{N}\langle\varphi_m(\vec{x}_1)\varphi_n(\vec{x}_2)|\, r_{12}^{-1}\left(|\varphi_m(\vec{x}_1)\varphi_n(\vec{x}_2)\rangle - |\varphi_m(\vec{x}_2)\varphi_n(\vec{x}_1)\rangle\right)$$

$$= \frac{1}{2}\sum_{m}^{N}\sum_{n\neq m}^{N}\langle mn|mn\rangle - \langle mn|nm\rangle \tag{2.20}$$

We have introduced the double-bar integral notation in eq. (2.20); its exact definition is eq. (2.19).

Putting together eq. (2.13) and eq. (2.20), we obtain the expectation value of the Hamiltonian for the Slater determinant:

$$E_0 \approxeq \langle\Psi|\hat{H}|\Psi\rangle = \sum_{m}^{N}\langle m|\hat{h}_1|m\rangle + \frac{1}{2}\sum_{m}^{N}\sum_{n\neq m}^{N}\langle mn|mn\rangle - \langle mn|nm\rangle \tag{2.21}$$

Notice that we still have no criteria for choosing a set of spin orbitals $\{\varphi_i\}$ except for orthonormality. With that being the only constraint, if we systematically vary the $\{\varphi_i\}$ until the energy E_0 reaches minimum. The resulting equations are a set of effective one-particle

eigenfunction and eigenvalue pairs:

$$\hat{F}(\vec{x}_i)\,|\varphi_m(\vec{x}_i)\rangle = \varepsilon_m\,|\varphi_m(\vec{x}_i)\rangle \tag{2.22}$$

where $\{\varepsilon_m\}$ are energies of the spin orbitals and $\hat{F}$ is the Fock operator which is a version of eq. (2.1) for individual spin orbitals:

$$\hat{F}(\vec{x}_i) = \hat{h}_1(\vec{x}_i) + \hat{J}(\vec{x}_i) - \hat{K}(\vec{x}_i) \tag{2.23}$$

$$\hat{h}(\vec{x}_i) = -i\frac{1}{2}\nabla^2_{\vec{x}_i} - \sum_A \frac{Z_A}{r_{\vec{x}_i A}} \tag{2.24}$$

$$\hat{J}_1(\vec{x}_i) = \sum_m^N \langle \varphi_m(\vec{x}_i)\varphi_n(\vec{x}_j)|r_{12}^{-1}|\varphi_n(\vec{x}_j)\rangle \tag{2.25}$$

$$\hat{K}_1(\vec{x}_i) = \sum_m^N \langle \varphi_m(\vec{x}_j)\varphi_n(\vec{x}_i)|r_{12}^{-1}|\varphi_m(\vec{x}_j)\rangle \tag{2.26}$$

As before, $\hat{h}$ is the one-electron operator. We have split the two-electron term into the Coulomb operator $\hat{J}$ and the exchange operator $\hat{K}$.

The most common approach to solving eq. (2.22) is to further expand $\{\varphi_i\}$ into linear combinations of atomic orbitals (LCAO), which themselves are composed of finite basis sets. Essentially, the spatial component of the spin orbitals are expanded as a set of M atomic orbital (AO) basis functions $\{\chi_m u(\vec{x}_i)\}$:

$$\varphi_m = \sum_\mu^M C_{\mu m}\chi_\mu(\vec{x}_i) \tag{2.27}$$

$\{C_{m\mu}\}$ are known as molecular orbital (MO) coefficients and will play a key role later on. Choosing an appropriate basis set for a given system is a non-trivial problem as most properties of the system vary significantly depending on the choice of basis sets, and there are a multitude to choose from. However, even if we manage to use a complete orbital basis set, the energy term obtained from eq. (2.21), i.e. the HF total energy, is only an approximation of the true total electronic energy. This is because the single-particle orbital picture of HF essentially allows each

electron to move freely against an *average* electron charge distribution. However, electrons repel and must avoid each other, e.g. the presence and movement of an electron in dynamically influenced by other nearby electrons – their movements have to be *correlated.* In other words, a HF wavefunction overestimates the probability of finding two electrons close together, which in turn causes the aforementioned discrepancy in total energy. This energy error is appropriately called the *total correlation energy*. HF is thus usually known as an "uncorrelated" model, in contrast to correlated ones such as Configuration Interaction or Coupled Cluster. When one needs to work with large systems like metal-ligand complexes, polymers or quantum dots, extremely high computational cost precludes the use of most correlated models, except for one:

2.2 Density Functional Theory (DFT)

DFT is often considered the least computational intensive correlated model. In 1927, Thomas and Fermi made the first attempts to use the electron density as a fundamental quantity for calculating properties of a system. Their basic idea was replacing the complicated many-electron wavefunction of $3N$ variables (where N is the number of electrons in the system) with the much simpler 3-variable electron density $\rho(\vec{r})$. The electron density is a probability distribution that gives the chance of finding an electron in a particular region of space. Even in Hartree Fock theory, the electron density is the primary quantity of interest. Formal justification for DFT are warranted by Hohenberg-Kohn theorems,[8] upon which Kohn and Sham[9] developed the practical implementation of DFT for real systems.

2.2.1 Hohenberg-Kohn Theorems

The first Hohenberg-Kohn theorem states that the external potential $v_{\text{ext}}(\vec{r})$, and consequently the total energy of a system, is a unique functional of the total charge density $\rho(\vec{r})$. Conversely, a single charge density function cannot produce two different ground state energies, and therefore uniquely determines the Hamiltonian operator and the ground state energy:

$$E_o(\rho(\vec{r})) = \langle \Psi | \hat{H} | \Psi \rangle \tag{2.28}$$

Recall that the Hamiltonian consists of the kinetic energy $\hat{T}$, the electron-electron interaction potential $\hat{V}_{ee}$. The charge density thus also uniquely determine the kinetic energy and interaction potential, i.e. $\hat{T}(\rho(\vec{r}))$ and $\hat{V}_{ee}(\rho(\vec{r}))$ for any number of particles and any external potential. Such a remarkable statement can in fact be straightforwardly proved using *reductio ad absurdum*:

If the theorem wasn't true, there would exist two external potentials $v_{ext}(\vec{r})$ and $v'_{ext}(\vec{r})$ that give rise to the same ground state density $\rho_o(\vec{r})$, which in turn result in two disctinct Halmiltonian $\hat{H}$ and $\hat{H}'$. Thus, the associated ground state wavefunctions Ψ and Ψ', and the ground state energies E_o and E'_o would also be different. Using the variational principle, we have:

$$\begin{aligned} E_o = \langle \Psi | \hat{H} | \Psi \rangle &< \langle \Psi' | \hat{H} | \Psi' \rangle \\ &< \langle \Psi' | \hat{H}' + v_{ext}(\vec{r}) - v'_{ext}(\vec{r}) | \Psi' \rangle \\ &< E'_o + \int \left[v_{ext}(\vec{r}) - v'_{ext}(\vec{r}) \right] \rho_o(\vec{r}) d\vec{r} \qquad (2.29) \\ E'_o = \langle \Psi' | \hat{H}' | \Psi' \rangle &< \langle \Psi | \hat{H}' | \Psi \rangle \\ &< \langle \Psi | \hat{H} + v'_{ext}(\vec{r}) - v_{ext}(\vec{r}) | \Psi \rangle \\ &< E_o + \int \left[v'_{ext}(\vec{r}) - v_{ext}(\vec{r}) \right] \rho_o(\vec{r}) d\vec{r} \qquad (2.30) \\ \Rightarrow\ E_o + E'_o &< E'_o + E_o \qquad (2.31) \end{aligned}$$

Equation (2.31), obtained by adding eq. (2.29) and eq. (2.30), is contradicting statement, therefore there must only be one and only one external potential functional for a given ground state charge density.

The second Hohenberg-Kohn theorem says that functional which maps charge densities to energies yields the lowest energy if and only if the ground state density is used. This theorem can also be trivially proved using the variational principle. It follows from the first theorem that a given candidate charge density ρ' would have its own Hamiltonian $\hat{H}'$ and wavefunction Ψ'. We can then use this candidate Ψ' as the trial wavefunction for the true Hamiltonian

$\hat{H} = \hat{T} + \hat{V}_{ee} + v_{ext}(\vec{r})$:

$$\begin{aligned}\langle \Psi' | \hat{H} | \Psi' \rangle &= \int \hat{T}[\rho'(\vec{r})] + \hat{V}_{ee}[\rho'(\vec{r})] + v_{ext}(\vec{r})\rho'(\vec{r})d\vec{r} \\ &= E[\rho'(\vec{r})] \geq \langle \Psi | \hat{H} | \Psi \rangle = E[\rho(\vec{r})] \end{aligned} \tag{2.32}$$

Note that these two theorems only tell us that a functional exists which maps the ground state charge density to the ground state energy of a system – they do not provide any guidance on how to find such functional.

2.2.2 The Kohm-Sham Approach

If the Hohenberg-Kohn theorems assure us of DFT's validity, the Kohn-Sham approach tells us how to actually apply DFT to electronic structure. Kohn and Sham[9] were the first to realize that earlier attempts to use functionals to map charge densities onto energies failed mostly because they had not been able to accurately capture the contribution from the kinetic energy term. Recall that Hartree Fock Approach was capable of calculating the kinetic energy of the noninteracting electrons exactly. Therefore, Kohm and Sham proposed a hybrid method where the starting "trial" charge density , whose orbitals are used to compute the kinetic energy contribution as rigorously as possible; then use functionals to deal with the unknown exchange and correlation effects in the real system.

Adapting directly from HF theory, the corresponding ground state wavefunction is given by a determinant of non-interacting single-electron orbitals $\{\varphi\}$:

$$\Psi_{KS} = \frac{1}{\sqrt{N!}} \det\left[\varphi_1(\vec{r}_1)\varphi_2(\vec{r}_2)\cdots\varphi_N(\vec{r}_N)\right] \tag{2.33}$$

Notably, the density of this non-interacting system is exactly the same as the density for the real system:

$$\rho_{KS}(\vec{r}) = \sum_i^N \varphi_i^* \varphi_i \equiv \rho(\vec{r}) \tag{2.34}$$

Then, the Hamiltonian is partitioned into three terms:

$$\hat{H}[\rho(\vec{r})] = \hat{T}[\rho(\vec{r})] + \hat{V}_{ee}[\rho(\vec{r})] = \hat{T}_{KS}[\rho(\vec{r})] + \hat{J}[\rho(\vec{r})] + E_{XC}[\rho(\vec{r})] \tag{2.35}$$

where the first two terms, which constitute the majority of the energy, are simply the kinetic and Coulomb exchange energy terms from HF:

$$\hat{T}_{KS}[\rho(\vec{r})] = -\frac{1}{2}\sum_{i}^{N}\langle\psi_i|\nabla^2|\psi_i\rangle \tag{2.36}$$

$$\hat{J}[\rho(\vec{r})] = \frac{1}{2}\iint\frac{\rho(\vec{r_1})\rho(\vec{r_2})}{r_{12}}d\vec{r_1}d\vec{r_2} \tag{2.37}$$

The third and much-smaller term is the difference between energies of the non-interacting system and the real one, and is called the exchange-correlation energy:

$$\hat{E}_{xc}[\rho(\vec{r})] = \left(\hat{T}[\rho(\vec{r})] - \hat{T}_{KS}[\rho(\vec{r})]\right) + \left(\hat{V}_{ee}[\rho(\vec{r})] - \hat{J}[\rho(\vec{r})]\right) \tag{2.38}$$

The total energy of the real interacting system is:

$$E_{xc}[\rho(\vec{r})] = \int v_{\text{ext}}(\vec{r})\rho(\vec{r})d\vec{r} + \hat{T}_{KS}[\rho(\vec{r})] + \hat{J}[\rho(\vec{r})] + \hat{E}_{xc}[\rho(\vec{r})] \tag{2.39}$$

Consequently, ground state energy can be obtained by varying the single-particles orbitals of the Kohn-Sham wavefunction, analogous to the HF's SCF procedure, except the one-particle Fock operator has been replaced by the one-particle Kohn-Sham operator:

$$\hat{F}_{KS} = -\frac{1}{2}\nabla^2 + \int\frac{\rho(\vec{r_2})}{r_{12}}d\vec{r_2} + v_{\text{ext}}(\vec{r_1}) + v_{xc}(\vec{r_1}) \tag{2.40}$$

$$v_{xc}(\vec{r_1}) = \frac{\partial}{\partial\rho(\vec{r})}E_{xc}[\rho(\vec{r})] \tag{2.41}$$

If $E_{xc}[\rho(\vec{r})]$ is explicitly known, the true energy of this interacting system can be computed exactly. Unfortunately in practice, only approximate functionals are available and currently no procedure exists to systematically improve their accuracy. Although the contribution of E_{xc} to a system's total energy is relatively small, its impact on other properties is quite dramatic and thus cannot be

ignored, as demonstrated in Chapter 4.

2.3 Time-Dependent Hartree-Fock/Density Functional Theory

The quantum mechanical treatment of any molecular process first starts with finding the initial time-independent wavefunction to represent the system involved. Assuming this initial wavefunction has been solved self-consistently to obtain the ground-state electronic wavefunction, the system by itself would remain in such ground state indefinitely. The system would only change in response to an external perturbation such as a laser or electric field, which can be described as a time-dependent potential in the Hamiltonian. The direct approach to calculate how the system behaves is to solve the time-dependent Schrödinger equation (TDSE). Nevertheless, the exact solution of the full TDSE is prohibitively expensive and only applicable for small systems. The time-dependent Hartree-Fock (TDHF), first proposed by Dirac in 1939, is a much more manageable approximation to the TDSE. Analogous to the time-independent counterpart, TDHF assumes that an N-electron system can always be represented by a single Slater determinant composed of N time-dependent single-particle orthonormal orbitals $\{\varphi(\vec{r},t)\}$:

$$\Psi(t) = \frac{1}{\sqrt{N!}} \det\left[\varphi_1(\vec{r}_1,t)\varphi_2(\vec{r}_2,t)\cdots\varphi_N(\vec{r}_N,t)\right] \tag{2.42}$$

Apply the Dirac-Frenkel time-dependent variational principle to this approximate wavefunction:

$$\langle\partial\Psi|i\frac{\partial}{\partial t} - \hat{H}_{el}|\Psi\rangle = 0 \tag{2.43}$$

And we obtain the TDHF equation:

$$i\frac{\partial}{\partial t}|\varphi_i\rangle = \hat{F}(t)|\varphi_i\rangle \tag{2.44}$$

Taking the complex conjugate of the above equation, we have:

$$-i\frac{\partial}{\partial t}\langle\varphi_i| = \langle\varphi_i|\hat{F}(t) \tag{2.45}$$

where we have taken advantaged of the fact that $\hat{F}(t)$ is Hermitian. The one-particle density operator is defined as:

$$\hat{\Gamma}(t) = \sum_{i}^{\text{occ}} |\varphi_i\rangle \langle\varphi_i| \tag{2.46}$$

Combining eq. (2.44) and eq. (2.46), we can easily obtain:

$$i\frac{\partial}{\partial t}\hat{\Gamma}(t) = \hat{F}(t)\hat{\Gamma}(t) - \hat{\Gamma}(t)\hat{F}(t) = \left[\hat{F}(t), \hat{\Gamma}(t)\right] \tag{2.47}$$

If we expand the molecular orbitals into a set of M time-independent atomic orbital basis $\{|\lambda\rangle\}$:

$$|\varphi_i\rangle = \sum_{\lambda}^{M} C_{\lambda,i}(t) |\lambda\rangle \tag{2.48}$$

The density matrix **P** in that same AO basis has elements of the form:

$$P_{\lambda\sigma}(t) = \sum_{i}^{\text{occ}} C_{\lambda,i}(t) C^*_{\sigma,i}(t) \tag{2.49}$$

eq. (2.46) could then be expressed as:

$$\hat{\Gamma}(t) = \textstyle\sum_i^{\text{occ}} \sum_{\lambda,\sigma} C_{\lambda,i}(t) C^*_{\sigma,i}(t) \tag{2.50}$$

$$= \textstyle\sum_{\lambda,\sigma} P_{\lambda\sigma}(t) |\lambda\rangle \langle\sigma| \tag{2.51}$$

Substituting section 2.3 above into eq. (2.47), we have:

$$i\sum_{\lambda,\sigma} \frac{\partial}{\partial t} P_{\lambda\sigma}(t) |\lambda\rangle \langle\sigma| = \sum_{\lambda,\sigma} \hat{F}(t) P_{\lambda\sigma}(t) |\lambda\rangle \langle\sigma| - \sum_{\lambda,\sigma} P_{\lambda\sigma}(t) |\lambda\rangle \langle\sigma| \hat{F}(t) \tag{2.52}$$

Multiplying the above equation by $\langle\mu|$ from the left and $|\nu\rangle$ from the right, we get:

$$i\frac{\partial}{\partial t} P_{\mu\nu}(t) = \sum_{\lambda} \langle\mu| \hat{F}(t) |\lambda\rangle P_{\lambda\nu}(t) - \sum_{\sigma} P_{\mu\sigma}(t) \langle\sigma| \hat{F}(t) |\nu\rangle \tag{2.53}$$

We can immediately recognize that $\langle\mu|\,\hat{F}(t)\,|\lambda\rangle$ is an element of the Fock matrix, $F_{\mu\lambda}$ in the AO basis,; and rewrite eq. (2.53) as:

$$i\sum_{\lambda,\sigma}\frac{\partial}{\partial t}P_{\lambda\sigma}(t) = \sum_{\lambda}F_{\mu\lambda}P_{\lambda\nu}(t) - \sum_{\sigma}P_{\mu\sigma}(t)F_{\sigma\nu}(t) \tag{2.54}$$

Since atomic basis functions are typically not orthonormal, i.e. the overlap matrix $\mathbf{S} = \langle\mu|\lambda\rangle$ is not the identity, we need to transform our density and Fock matrices into an orthonormal basis by a transformation matrix $\mathbf{V}$:

$$\mathbf{P}' = \mathbf{V}\mathbf{P}\mathbf{V}^T \qquad\qquad \mathbf{F}' = \mathbf{V}^{-T}\mathbf{F}\mathbf{V}^{-1} \tag{2.55}$$

using either Löwdin ($\mathbf{V} = \mathbf{S}^{1/2}$) or Cholesky ($\mathbf{V}^T\mathbf{V} = \mathbf{S}$) transformation. Once converted to this orthonormal basis, the time propagation of the density matrix is governed by the TDHF equation:

$$i\frac{\partial}{\partial t}\mathbf{P}(t) = [\mathbf{F}'(t), \mathbf{P}'(t)] \tag{2.56}$$

The TDDFT has the same form as the TDHF equation in eq. (2.56), except that the HF exchange potential has been replaced by the xc potential.

Several methods exist to integrate and solve the TDHF equation as shown in eq. (2.56): 4^{th}-order Runge-Kutta, unitary exponential midpoint, high-order Magus.[10] Our implementation of the TDHF utilized a version of the unitary exponential midpoint method called the modified midpoint and unitary transformation (MMUT).[11,12] Midpoint here refers to the computation of the Fock matrix at the midpoint of the time step, hence any linear change in the density matrix would be accounted for. If $\mathbf{P}'$ is evolved over a time step Δt small enough so that $\mathbf{F}'$ can be assumed to remain constant, the formal solution for eq. (2.56) can be expressed as:

$$\begin{aligned}\mathbf{P}'(t+\Delta t) &= \hat{\mathbf{U}}(2\Delta t)\mathbf{P}'(t)\\ &= \exp\left(-i[\mathbf{F}'(t), \mathbf{P}'(t)]2\Delta t\right)\cdot\mathbf{P}'(t) &(2.57)\\ &= \exp\left(-i\mathbf{F}'(t)2\Delta t\right)\cdot\mathbf{P}'(t)\cdot\exp\left(i\mathbf{F}'(t)2\Delta t\right) &(2.58)\end{aligned}$$

where we have introduced the time-evolution operator $\hat{\mathbf{U}}(t) = \exp\left(-i\mathbf{F}'(t)2\Delta t\right)$ and applied the

Baker-Campbell-Hausdorff formula $e^{[X,Y]}Y = e^X Y e^{-X}$ to eq. (6.2) and obtained eq. (6.3) as our principle working equation. $\hat{\mathbf{U}}(t)$ can then be constructed from the eigenvectors of the Fock matrix:

$$\hat{\mathbf{U}}(t) = \mathbf{C}(t) \exp\left[-i2\Delta t\, \varepsilon(t)\right] \mathbf{C}^\dagger(t) \tag{2.59}$$

$$\varepsilon(t) = \mathbf{C}^\dagger(t) \cdot \mathbf{F}'(t) \cdot \mathbf{C}(t) \tag{2.60}$$

In relativity, movement is continuous, causally determinate and well defined, while in quantum mechanics it is discontinuous, not causally determinate and not well defined.

David Bohm

3

Motivation: Resonant Photoelectric Spectroscopy

3.1 Background

Of immense interest in quantum chemistry is the group of processes conjointly known as electron or charge transfer (ET or CT). CT is a prototypical process in nature,[13] the driving mechanism behind a multitude of phenomena, ranging from the colors of gemstones or pigments to photosynthesis and displays in electronic devices. Realistically, a major subset of CT processes only involve the electrons and occur on the femtosecond timescale. These processes are ideal candidates for electronic structure theory, since certain approximations, e.g. Born-Oppenheimer, are only valid at this timescale, thus significantly alleviate the efforts to model these ultrafast processes without a consequential decrease in accuracy. And last but not least, due to its direct photovoltaic applications, ultrafast photoinduced CT has been propelled into the limelight of recent energy and semiconductor research.[14,15,16,17,18,19,20,21] However, the ultra-fast nature of these processes also make them quite challenging to study experimentally. Resonance

photoemission spectroscopy (RPES) is among the few techniques that can directly probe ultrafast CT.

Resonant Auger is an extension of near-edge X-ray absorption fine structure (NEXAFS) and possesses the same chemical and site specificity.[22,23] Resonant Auger spectroscopy is an excitation-decay technique, where the core-hole lifetime serves as a delay (on the order of a few femtoseconds for 1s of carbon, nitrogen and oxygen) during which the system relaxes. Provided that the involved core orbitals have sufficient spatial overlap with the LUMO, the lowest energy resonance in the NEXAFS maintains some analogy to an optical bandgap excitation for the electron, with the notable exception that a localized atomic core hole is produced rather than a delocalized valence hole. By evaluating the energy and intensity of the core-hole decay products, resonant Auger spectroscopy can thus be used to probe the electronic structure of this excitation, without the complexities of pump-probe techniques.

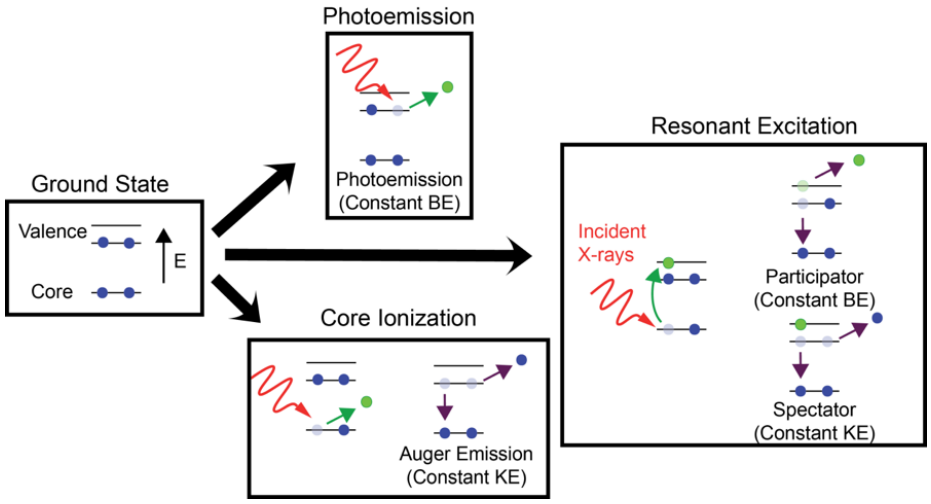

Figure 3.1.1: Decay pathways for different types of X-ray excitations. Auger and spectator pathways emit electrons at constant kinetic energy (KE), while photoemission and participator pathways emit at constant binding energy (BE). Green represents the photo-excited electron and purple arrows represent Auger processes

Figure 3.1.1 shows the decay paths that appear in the photoemission spectrum for resonant and non-resonant excitations. For resonant excitations (fig. 3.1.1's right panel), the excited electron can either participate in the Auger decay process (participator decay) or spectate the

Auger decay process (spectator decay). The presence of the spectator electron in the spectator Auger decay will shift the final state energy relative to the non-resonant Auger pathway, which is reflected experimentally as a shift in the kinetic energy of the outgoing Auger electron (spectator shift). The spectator shift is mainly associated with the screening of the double-hole Auger final state by the excited electron and therefore provides a qualitative measure of the spatial overlap of the excited state wavefunction with the excited atom. Initial inspection suggested that our RT TD-DFT approach should be able to capture the activity of the spectator electron and verify the spectator shift inferred experimentally.

3.2 Methodology

We chose two donor/acceptor-type polymers with which to examine LUMO structure: poly[2,1,3-benzothiadiazole-4,7-diyl[4,4-bis(2-ethylhexyl)-4H-cyclopenta[2,1-b:3,4-b']dithiophene-2,6-diyl]] (PCPDTBT, fig. 3.2.1a) and poly[[9-(1-octylnonyl)-9H-carbazole-2,7-diyl]-2,5-thiophenediyl-2,1,3-benzothiadiazole-4,7-diyl-2,5-thiophenediyl] (PCDTBT, fig. 3.2.1b). We chose these materials because both polymers belong to the newer generation of materials being used in organic photovoltaics. They both have alternating electron-donating (dithiophene or carbazole for PCPDBT and PCDTBT, respectively) and electron-accepting (benzothiadiazole) units along the polymer backbone, and are known to make efficient organic photovoltaic devices.[24,25] The internal quantum efficiency (IQE) for PCDTBT devices has been reported to be nearly 100%,[25] while the IQE for PCPDTBT devices is more typically 70%.[26] In spite of having such similar structures, PCDTBT and PCPDTBT display such distinct charge transfer characteristics, making them prime candidates to be compared via resonant Auger spectroscopy.

Since studying a full thin-film polymer is not yet computationally feasible, we approximate the alkyl chains with methyl groups and first focused on the singly and doubly-repeat units, i.e. "monomer" and "dimer" representation of these polymers. DFT is then used to optimize the polymers for ground state structures and energies. Furthermore, Mulliken population analysis is employed to screen for potential donor-acceptor MOs for the first resonant excitation. All DFT calculations were performed using the B3LYP exchange correlation functional[27,28,29] and

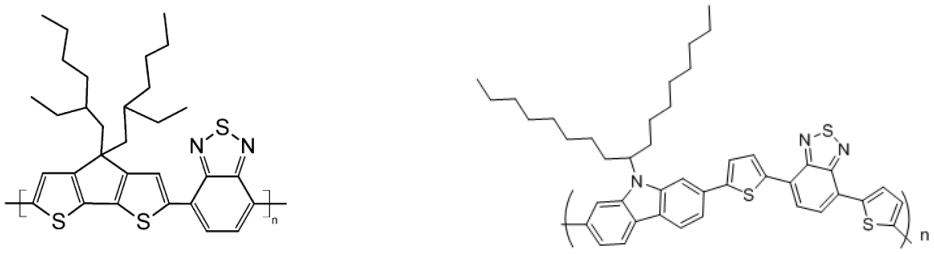

(a) PCPDTBT **(b)** PCDTBT

Figure 3.2.1: Molecular structure of polymers

6-31G(d) basis set with the development version of the GAUSSIAN software suite.[30]

3.2.1 First Trial: RT TD-DFT

For the both polymers, the core donor candidates are immediately identifiable as the only MOs with virtually degenerate energies and electron density completely localized on the N atoms to either side of the S atoms in the repeat unit (see the "hole" orbitals plotted on the optimized geometry of the monomers in fig. 3.2.3). However, several candidates exist for the acceptor MOs: not only does the LUMO but several orbitals directly following the LUMO also have electron density delocalized over the benzothiadiazole unit, in which also lie the N atoms whose core 1s electron would be excited. To simulate this initial excitation, we would promote the electron from one of the core 1s orbitals to another unoccupied orbital. In both units, we choose the LUMO as the accepting MOs since it has the most contribution from the N atoms' atomic orbitals ($\approx 30\%$). Since the energy gap between the core 1s orbitals and most of the low-lying unoccupied ones is so large (380-390 eV), having higher spatial overlap is likely to indicate higher correlation between two MOs. So, at time $t = 0$, starting from the optimized ground state geometry, we prepare the initial resonant excited state by promoting the core 1s electron of the N atom to LUMO, then let the resulted coherent wave packet propagate and evolve in time via RT TD-DFT. To analyze the electronic dynamics, the time-dependent density is projected on the ground state orbital space:

$$n_k(t_i) = \mathbf{C}_k^\dagger(0)\mathbf{P}(t_i)\mathbf{C}_k(0) \tag{3.1}$$

where $\mathbf{C}_k(0)$ is the k^{th} eigenvector of the initial $(t = 0)$ Kohn-Sham matrix.[11] Section 3.2.1 shows the time-evolution of the photoexcited LUMO electron and core hole in the PDPCTBT monomer. The expected lifetime of the core hole is less than 6 fs, while the charge transfer of the excited electron should happen in 1 - 3 fs. What we observed in the simulation was quite contradictory: the core hole remained perfectly stable up until 30 fs while the excited electron oscillated perpetually between the LUMO and LUMO+1 orbitals. The excessive energy only causes the HOMO electron to dissipate slowly – there is absolutely interaction between the core hole and the HOMO electron, or any other electron for that matter, as expected of the spectator process. We also attempted another simulation by promoting the core 1s electron to the LUMO+3 section 3.2.1 orbital due to its having the second highest contribution from the N's AOs but the result is largely the same: the excited electron also oscillates, albeit at a lower frequency, to an unoccupied MO much higher in energy while the core hole remains stable. To be thorough, simulations with core 1s to LUMO+1 and LUMO+2 swap were also carried out but to no avail. It appears RT TD-DFT is unable to capture the spectator shift phenomenon.

3.2.2 Second Trial: ES LR TD-DFT

Still determined to understand the electronic characteristics for each polymer, we resorted to the energy-specific linear response (ES LR) formalisms of TD-DFT[31] where excited states are generated by vertical excitations from the core orbitals (1s) of the N atoms in each PCPDTBT and PCDTBT molecule (see next chapter for a brief overview of ES LR TD-DFT). The results from ES LR TD-DFT calculations for both polymer are compared against the experimental N K-edge NEXAFS spectrum in fig. 3.2.3. At first glance, it seems the first X-ray resonance for both PCPDTBT and PCDTBT is best described as a linear combination of multiple single-electron excitations, weighted by their respective oscillator strengths. The LUMO of PCDTBT has similar overlap with the N atoms in the benzothiadiazole unit when compared with PCPDTBT. Subsequent frequency calculations were performed to verify the minima of the potential energy surface. As aforementioned, the acceptor MOs are spread out over several atoms, including the same N atom from which the 1s electron is excited. Thus the Mulliken population density localized at the N atom site resolved from the excited state wavefunction is a reasonable approximation of the spatial overlap between the wavefunction and excited N atom. To better

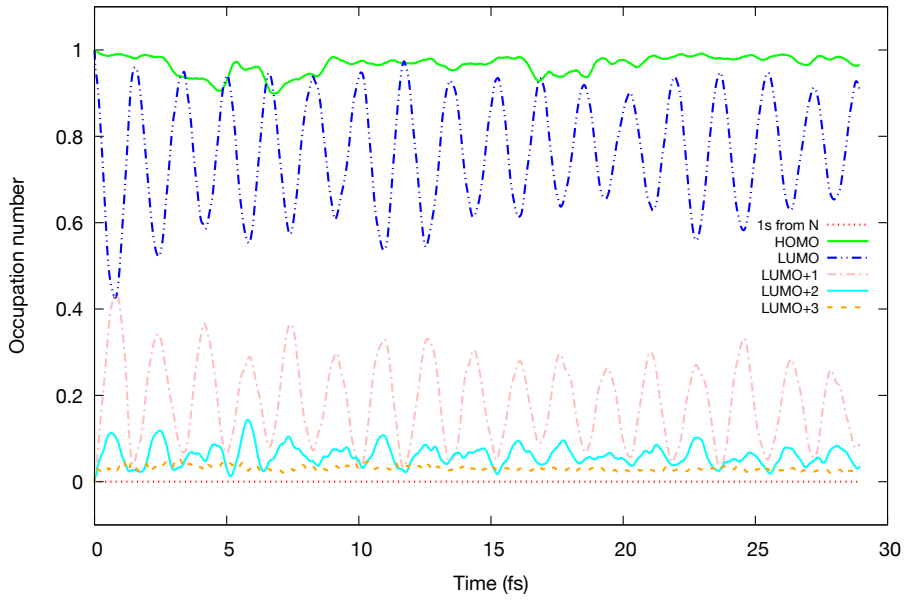

(a) Core 1s $\longrightarrow$ LUMO (29% contribution from N's AOs)

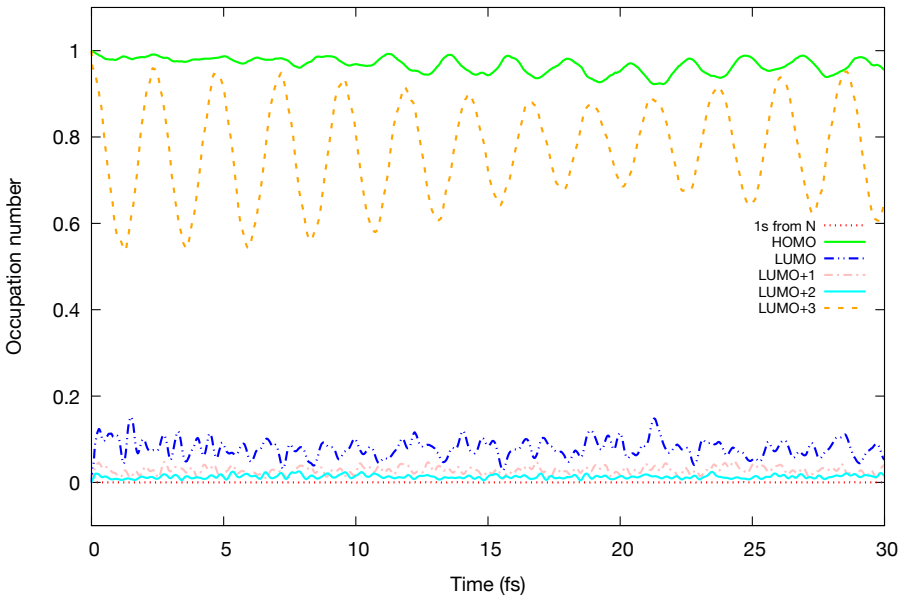

(b) Core 1s $\longrightarrow$ LUMO+3 (18% contribution of N's AOs)

Figure 3.2.2: Time-dependent electronic density projected on the ground state molecular orbital space of photoexcited PCPDTBT monomer following the core 1s excitation at time $t = 0$.

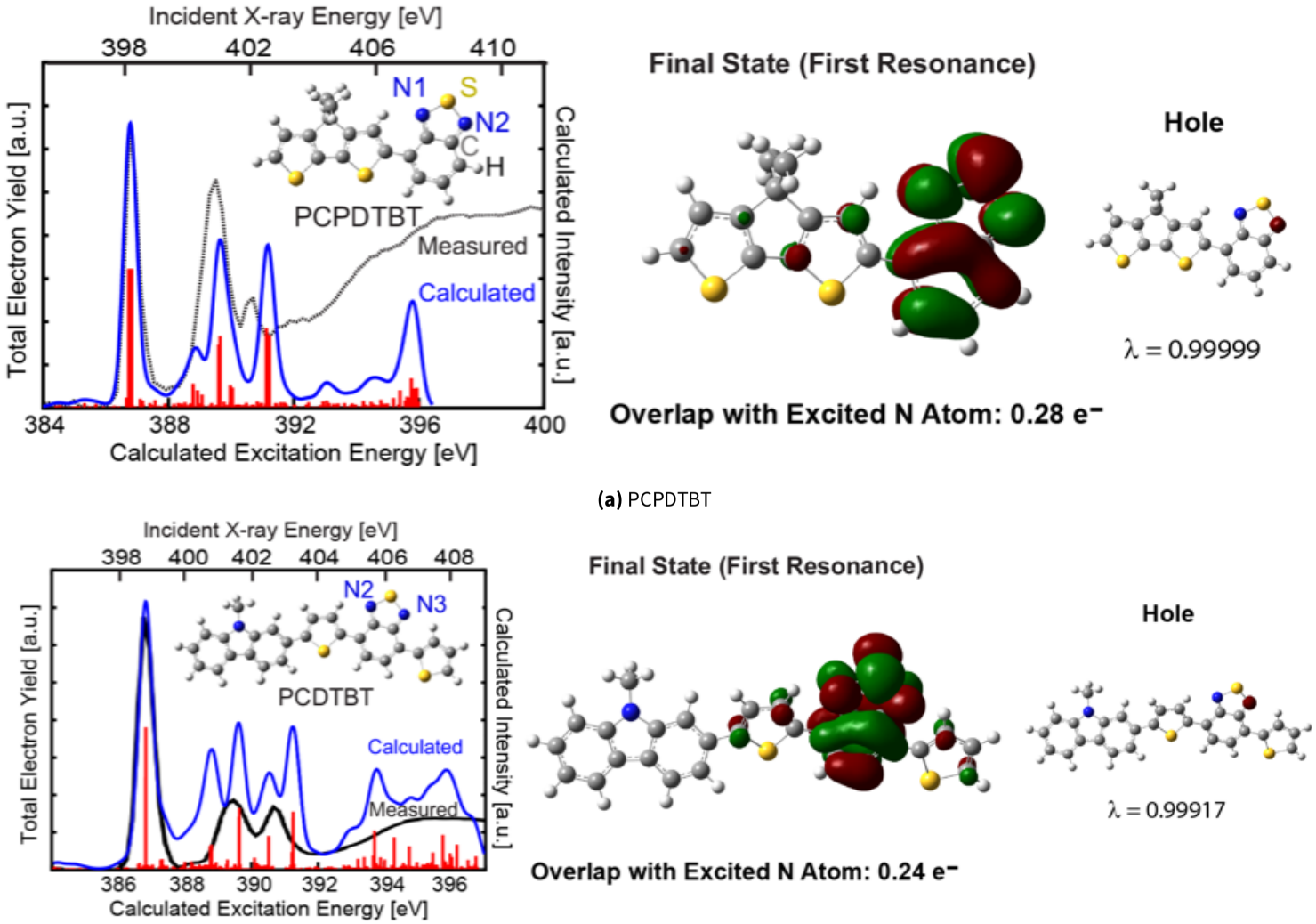

Figure 3.2.3: LEFT: ES-LR-TDDFT calculated N 1s x-ray absorption spectrum of the polymers' repeat unit. The red lines are TD-DFT solutions corresponding to excitations from N 1s to unoccupied MOs. X-ray absorption spectra (blue solid lines) are simulated by convolving the vertical transition energies and oscillator strengths with Gaussian functions characterized by a full width at half maximum (FWHM) of 0.2 eV. For comparison, the black dashed line shows the measured NEXAFS spectrum, red-shifted by approximately 11 eV for both polymers. The DFT-optimized geometry is inset. RIGHT: The NTO for the excited state corresponding to the first resonance along with the corresponding hole and λ. The spatial overlap between the photo-excited electron and the excited N atom is denoted for each structure.

visualize and interpret the excited state corresponding to the first resonance in the experimental NEXAFS spectra, we utilize natural transition orbitals (NTOs),[32] which succinctly describe the electronic transitions in terms of an expansion into single-particle orbitals (electron and hole). The eigenvalues (λ) obtained from diagonalizing the single-particle transition density matrix reflect the contribution of the associated single particle-hole excitations to the NTO; typically this value is $98 - 99\%$, indicating a single particle-hole transition dominates the excitation as expected. The measured spectator shift for the first resonance of PCDTBT (1.6 ± 0.3 eV) is within the range of values predicted by our TD-DFT calculations and the final-state effect screening model ($1.2 - 1.6$ eV). The spectator shift is identical to that exhibited by PCPDTBT (1.6 ± 0.4 eV), which matched the predicted value of $1.8 - 1.9$ eV. Using this experimental technique, we have confirmed the similarities in the excited states of PCPDTBT and PCDTBT predicted by theoretical calculations.

3.3 Discussion

N 1s X-ray absorption spectra (XAS) were calculated for PCDTBT and PCPDTBT using ES LR TD-DFT and showed good agreement with the experimental NEXAFS spectra. The more interesting question is why RT TD-DFT failed to describe the spectator shifts. We can only make a few educated guesses as follow. The relaxation of the spectator electron might actually involve two electrons explicitly, so the single-particle framework of DFT could not directly describe it. Short of switching to a higher and more expensive level of theory such as Configuration Interaction, little else can be done.

There are lower hanging fruits, however, such as changing the basis set and exchange functionals. We did explore the use of the cc-pVDZ basis, which contains an additional set of atomic orbitals for core levels. We found little improvement over 6-31G(d) to justify the increase in computing time. However, since XAS probes core electron excitations, flexible basis sets with a reasonable number of core functions, such as the cc-pCVTZ basis set, could potentially improve the description of core orbital relaxation upon excitation.

We also repeated the ES LR TD-DFT calcutions for the single repeat unit of both polymers using the BHandHLYP functional. The obtained spectra shown in section 3.3 not only are less

red-shifted than those using B3LYP but the major peaks also match up better with experimental data. Last but not least, experimentally these polymers are thin-film submerged

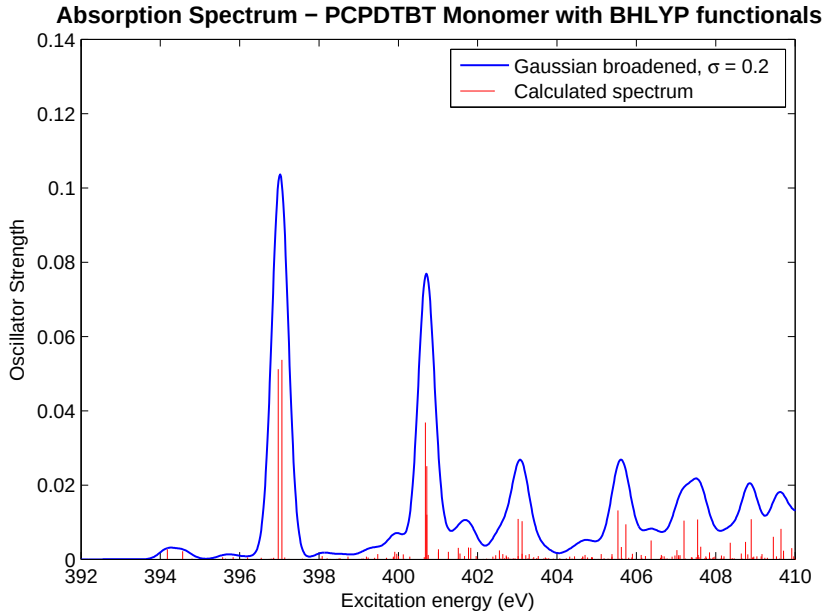
Absorption Spectrum − PCPDTBT Monomer with BHLYP functionals
Gaussian broadened, σ = 0.2
Calculated spectrum
Oscillator Strength
Excitation energy (eV)
0.14
0.12
0.1
0.08
0.06
0.04
0.02
0
392
394
396
398
400
402
404
406
408
410

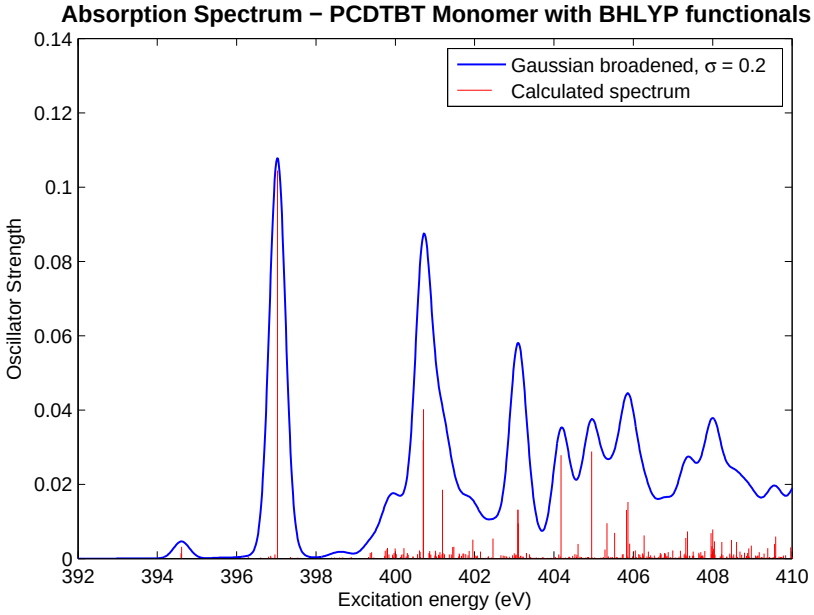
Absorption Spectrum − PCDTBT Monomer with BHLYP functionals
Gaussian broadened, σ = 0.2
Calculated spectrum
Oscillator Strength
Excitation energy (eV)
0.14
0.12
0.1
0.08
0.06
0.04
0.02
0
392
394
396
398
400
402
404
406
408
410

In relativity, movement is continuous, causally determinate and well defined, while in quantum mechanics it is discontinuous, not causally determinate and not well defined.

David Bohm

4

The Impact of Functionals in DFT Calculations

As alluded to earlier, before making any attempt at improving TD-DFT in studying ultrafast CT processes, we need to address the colloquial "elephant in the room": the arbitrary nature of choosing a density functional in any DFT calculation.

As mentioned above, the RPES technique studied in Chapter 3 is an extension of NEXAFS, which is particularly effective at elucidating structural information for individual atoms, by virtue of their high sensitivity to oxidation state, local geometry, bonding characteristics, and especially the ability to probe unoccupied electronic states. Such knowledge is integral to a solid understanding of its macroscopic and microscopic behaviors.[33,34,35,36] XAS in general studies transitions of core electrons into bound or continuum states as excited by absorption of X-ray photons. The resulted absorption spectra consist of pronounced fine features with sharp edges similar to fig. 4.0.1, grouped and labeled according to which core orbital the electrons come from; e.g K-edge, L_1-edge, L_2-edge for $1s$, $2p_{1/2}$, $2p_{3/2}$ electrons, respectively.[22] Each of these fine structures are divided into two regions: the narrow and intense peaks within 30-50 eV before (the

Pre-Edge) and after the absorption edge constitute the Near Edge X-ray Absorption Fine Structure (NEXAFS) or X-ray Absorption Near Edge Structure (XANES) region and correspond to the excitations of a core electron to give a bound state below the ionization continuum. This region is easier to measure, provides information about the unoccupied orbitals and bonding chemistry of the donating atom. At higher energy are weak oscillations which correspond to Extended X-ray Absorption Fine Structure (EXAFS) and arise from excitation to states above the ionization continuum and subsequent scattering of the photoelectron by its environment. Typically, EXAFS region is used with metal-containing system to determine metal–ligand bond distances and coordination numbers, while the NEXAFS/XANES region is used to obtain electronic structure information about a given species, i.e. a simple "fingerprint" to identify its presence.

Figure 4.0.1: Sample XAS Spectrum[1]

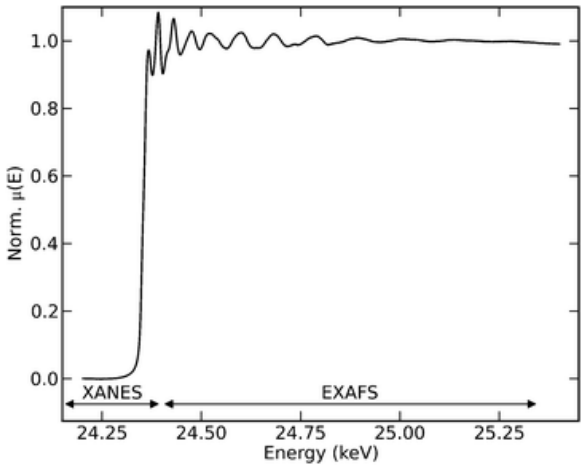

Given its widespread significance applicability, we would like to formally calibrate the performance of TDDFT method for modeling NEXAFS with an emphasis on the dependence on density functionals and basis sets. We will examine the different levels of theory to better characterize the ability of standard density functionals to model NEXAFS. We calculate the K-edge spectra of carbon, nitrogen, and oxygen and compare our results to available experimental data. This will provide a dependable benchmark for TDDFT and highlight its utility for modeling core excitations of light elements.

4.1 Methodology

In this study,[6] we utilized the linear response TDDFT approach, in which the excitation energies ω are obtained as solutions to the non-Hermitian eigenvalue equation:

$$\begin{bmatrix} \mathbf{A} & \mathbf{B} \\ \mathbf{B} & \mathbf{A} \end{bmatrix} \begin{bmatrix} \mathbf{X} \\ \mathbf{Y} \end{bmatrix} = \omega \begin{bmatrix} 1 & 0 \\ 0 & -1 \end{bmatrix} \begin{bmatrix} \mathbf{X} \\ \mathbf{Y} \end{bmatrix} \tag{4.1}$$

with the matrices **A** & **B** are given by:

$$A_{ia,jb} = \delta_{ij}\delta_{ab}(\varepsilon_a - \varepsilon_b) + \langle ia|jb\rangle - \langle ib|ja\rangle - a\langle ib|ja\rangle + \langle ia|f_{xc}|jb\rangle \tag{4.2}$$

$$B_{ia,jb} = \langle ia|jb\rangle - a\langle ij|ba\rangle + \langle ia|f_{xc}|bj\rangle \tag{4.3}$$

We can calculate the first order electron density responses **X** and **Y** by solving the above system of linear equations. In the two-electron integral terms, occupied and virtual molecular orbitals (MO) are indexed by i, j and a, b respectively. The scaling factor a in front of the HF exchange integral has value between 0 and 1 for hybrid DFT while becoming zero for pure kernels. The response of the exchange-correlation (xc) kernel is given as:

$$(ia|f_{xc}|jb) = \iint \varphi_i^*(r)\varphi_a(r)\frac{\delta^2 E_{xc}}{\delta\rho(r)\,\delta\rho(r')}\varphi_j^*(r')\varphi_b(r')\,dr\,dr' \tag{4.4}$$

Solving the system of linear equations as shown in eq. (4.1) yields the first order electron density responses **X** and **Y**. For real orbitals, eq. (4.1) can be dimensionally reduced in half to a Hermitian eigenvalue problem:

$$(\mathbf{A}-\mathbf{B})^{1/2}(\mathbf{A}+\mathbf{B})(\mathbf{A}-\mathbf{B})^{1/2}\mathbf{T} = \omega^2\mathbf{T} \tag{4.5}$$

$$\mathbf{T} = (\mathbf{A}-\mathbf{B})^{1/2}(\mathbf{X}+\mathbf{Y}) \tag{4.6}$$

Since **A** and **B** include all transitions between occupied and unoccupied orbitals, technically, LR-TDDFT can readily be used to study high-energy excitation such as those observed with NEXAFS. However, every single excited state before those high-energy ones of interest must also be solved. The size of these two matrices is roughly $(N_{occ} \times N_{unocc})^2$, where N_{occ} and N_{unocc} are

numbers of occupied and unoccupied MOs, so such a catch-all approach can become too computationally expensive, even for low-Z systems. We have previously introduced an energy-specific approach to LR-TDDFT (ES LR-TDDFT),[31] which selectively solves for solutions to the LR-TDDFT equations above a predefined energy threshold while maintaining the orthogonality between excited states and the ground state. This is done by constructing and expanding a fixed number of trial vectors above the energy threshold to be used during simple yet effective Davidson-like diagonalizations.

The procedure is summarized as following. Let's say we need to find M excited states with energies above ω_o. We first project $(\mathbf{A}+\mathbf{B})$ and $(\mathbf{A}-\mathbf{B})$ onto a subspace of trial vectors $\mathbf{C} = \{\mathbf{b}_1, \ldots, \mathbf{b}_l\}$ generated by sampling the Koopmans' MO transitions. $l = 4M$ trial vectors are generated during the first step.

$$\tilde{\mathbf{M}}^{+} = \mathbf{C}^T(\mathbf{A}+\mathbf{B})\mathbf{C} \tag{4.7}$$

$$\tilde{\mathbf{M}}^{-} = \mathbf{C}^T(\mathbf{A}-\mathbf{B})\mathbf{C} \tag{4.8}$$

$$\tilde{\mathbf{M}} = (\tilde{\mathbf{M}}^{-})^{1/2}(\tilde{\mathbf{M}}^{+})(\tilde{\mathbf{M}}^{-})^{1/2} \tag{4.9}$$

then diagonalize $\tilde{\mathbf{M}}$ to get the eigenvalues $\tilde{\omega}_M$ & eigenvectors $\tilde{\mathbf{MT}}$. The predefined requirement for excitation energy $\tilde{\omega}_M = \{\tilde{\omega}_i | \tilde{\omega}_i \geq \omega_o\}$ will help us narrow down the choices of the qualifying candidates and their associated $\tilde{\mathbf{T}}_M$, as well as generate the transition densities and transform them from this reduced space into approximate solutions in the full MO space (denoted by the prime notation):

$$\omega'_M = \tilde{\omega}_M \tag{4.10}$$

$$(\mathbf{X}'+\mathbf{Y}')_M = \mathbf{C}(\tilde{\mathbf{X}}+\tilde{\mathbf{Y}})_M \tag{4.11}$$

$$(\mathbf{X}'-\mathbf{Y}')_M = \mathbf{C}(\tilde{\mathbf{X}}-\tilde{\mathbf{Y}})_M \tag{4.12}$$

When errors of these approximate solutions, which is the norm of the residual vectors:

$$\mathbf{W}^L_M = (\mathbf{A}+\mathbf{B})(\mathbf{X}'+\mathbf{Y}')_M - \omega'_M(\mathbf{X}'-\mathbf{Y}')_M \tag{4.13}$$

$$\mathbf{W}^R_M = (\mathbf{A}-\mathbf{B})(\mathbf{X}'-\mathbf{Y}')_M - \omega'_M(\mathbf{X}'+\mathbf{Y}')_M \tag{4.14}$$

are below 10^{-6} au, the associated exicited states are considered converged. We can then construct new set of vectors for unconverged states, add them to **C**:

$$\mathbf{Q}_M^{L,R} = (\omega_M^{'} - \Delta\varepsilon)^{-1}\mathbf{W}_M^{L,R} \tag{4.15}$$

And restart from eq. (4.7) until we have obtained M converged states. Because convergence is tested in the full MO space, the solutions of the ES-TDDFT methods are exact within the TDDFT framework.

4.2 Results & Discussion

A total of 30 K- edge transitions for carbon, nitrogen, and oxygen (CO, CH_2O, C_2H_4, N_2, NH_3, NO_2) were calculated using ES-TDDFT with different functional and basis set combinations. Three family of electron basis sets were used: Pople 6-311+G(d,p),[37,38] Ahlrichs def2-TZVPD,[39,40,41,42] and Dunning aug-pVTZ.[43,44] In order to investigate the effect of core basis functions and diffuse functions, the singly and doubly augmented cc-pCVTZ basis sets have also been included.[45,46] Ground-state structures were optimized with the B3LYP functional and the def2-TZVP basis set. In order to investigate the effect of core basis functions and diffuse functions, the single and doubly augmented cc-pCVTZ basis have also been used. The commonly available functionals: BHandHLYP,[47] B3LYP,[48,49] PBE1PBE,[50,51] and BP86;[52,53] and two range-separated functionals: HSE06[54,55,56] and LC-ωPBE[57] have been included in this study.

Comparisons are made based on various types of errors as listed in tables 4.2.1 and 4.2.2. There are two group of error terms: absolute and shited. Because of inherent problems with DFT and the neglect of relativistic effects, DeBeer George et al.[58] have proposed that relative transition energies are more chemically relevant quantities than absolute transition energies when modeling core excitations. Therefore, we also apply a uniform shift to the calculated spectrum such that the lowest energy peak perfectly matches the experimental value, as is done in other studies.[59,60,61] The shifted errors are then calculated for the remaining transitions. All calculations were carried out using a development version of Gaussian[62] and compared with experimental results obtained from either gaseous XAS or inner-shell EELS.[63,64,65,66,67,68,69]

Table 4.2.1 shows the error analysis of predicted K-edge spectra with the ES LR TD-DFT

method. When absolute errors are considered, functionals with a larger percentage of HF exchange result in transition energies much closer to experimental values. This is consistent with trends seen in previous studies.[59,70] BHandHLYP has 50% HF exchange (the largest percentage of HF exchange among all DFT kernels considered here) and consistently outperforms the other functionals, in terms of absolute errors with respect to experimental results. The pure density functional (BP86), with no HF exchange, significantly underestimates the K-edge excitation energies by as much as ∼26 eV, compared to only 2-4 eV error by BHandHLYP and 11-17 eV error by B3LYP, PBE1PBE, and HSE06. The performance of BHandHLYP is likely attributed to the lower self-interaction error as compared to the other functionals,[71] and error cancellations arising from the fact that TDHF consistently overestimates the excitation energies by 15–22 eV. The two range-separated functionals tested, HSE06 and LC-ωPBE, are based off of the PBE functional and include short-range and long-range HF exchange, respectively. The HSE06 functional has comparable absolute errors to PBE1PBE (11–15 eV), but LC-ωPBE underestimates K-edge excitation energies by 18–24 eV. The inclusion of exact short-range exchange has been shown to reduce the self-interaction error and improve the description of core excitation energies while long-range exchange appears to be less important for core excitations.[71,72] Without the inclusion of short-range exchange, the transition energies calculated with LC-ωPBE are more similar to those calculated with the pure functional

Based on the shifted errors, all hybrid functionals are much improved. The pure functional is less reliable with errors as large as ∼4 eV. Unlike absolute transition energies, the magnitude of exact exchange among hybrid functionals does not appear to be the most important factor for reproducing relative transition energies. For example, the PBE1PBE functional has the lowest shifted errors (among the functionals that are not range-separated) for several of the basis sets tested. The shifted results for TDHF are still very poor, indicating the importance of electron correlation on core excitations. From the statistics of all K-edge excitations summarized in table 4.2.1, BHandHLYP clearly shows the best agreement with experimental values when absolute excitation energies are considered. When shifted results are used as in most computational practices, all hybrid functionals considered here show similarly good performance with HSE06 being the best choice, in terms of mean average errors and standard derivation. Table 4.2.1 also shows that absolute errors of K-edge excitations are less sensitive to the quality of valence basis, compared to the shifted results. Among the three split valence basis sets considered

in table 4.2.1, aug-cc-pVTZ results have a smaller standard deviation, compared to the other two sets.

Table 4.2.2 compares K-edge excitations using different basis sets with a focus on the importance of core and diffuse basis functions. The addition of more core functions seems to have little effect for these light elements as the excitation energies shift only slightly toward the experimental values. However, the average change due to these additional core functions does increase with atomic number. This suggests that core functions will be more important for heavier elements where the other functions in the set may not be capable of describing the core relaxation well. The shifted results are virtually unchanged with the addition of more core functions, differing by <0.01 eV. Diffuse functions have a slightly larger effect on the transition energies. An extra set of diffuse functions slightly increases the absolute error for all functionals, but is slightly reduced for TDHF. For the shifted spectra, the error is reduced for BHandHLYP and TDHF, but increases for all other methods with $<50\%$ HF exchange. Without a large portion of HF exchange, additional diffuse functions are not advantageous and lead to a worse description of the relative transition energies.

4.3 Conclusion

Six density functional kernels and various basis sets were used to evaluate the accuracy of ES-TDDFT for describing K-edge transitions of carbon, nitrogen, and oxygen. The results of 30 different transitions were compared against experimental values in the gas phase. There is a consistent improvement in the absolute values of the calculated excitation energies with increasing HF exchange.[59,70] Particularly, short-range exchange was shown to be an important component of any hybrid functional applied to core excitations. When shifted results are used, all hybrid functionals considered here show similarly good performance, with HSE06 being the best choice, in terms of mean average errors and standard deviation. For K-edge excitations of light elements, the choice of basis set does not appear to have a large effect on the absolute or shifted errors of the transition energies, and these errors are mostly dominated by the choice of functional. Although a second set of diffuse functions seems to increase the error of the shifted spectra for all functionals with $<50\%$ HF exchange

Table 4.2.1: Errors for All K-Edge Transitions, Using Different Basis Set Families

	K-edge Transition Data (eV)[a]									
Basis Set	Absolute Errors					Shifted Errors				
	Mean AE	RMS	Max AE	MSE	Std Dev	Mean AE	RMS	Max AE	MSE	Std Dev
					BP86					
6-311+G(d,p)	20.09	20.24	24.51	-20.09	2.46	1.68	1.82	2.71	-1.39	1.18
def2-TZVPD	19.93	20.09	24.54	-19.93	2.55	1.75	1.86	2.59	-1.22	1.41
aug-cc-pVTZ	20.45	20.59	24.79	-20.45	2.40	1.98	2.18	3.12	-1.97	0.94
					PBE1PBE					
6-311+G(d,p)	11.36	11.43	13.79	-11.36	1.23	0.58	0.73	2.20	-0.24	0.68
def2-TZVPD	11.21	11.30	13.80	-11.21	1.41	0.72	1.05	3.62	-0.06	1.05
aug-cc-pVTZ	11.60	11.65	13.80	-11.60	1.12	0.70	0.78	1.26	-0.67	0.40
					B3LYP					
6-311+G(d,p)	12.88	12.97	15.85	-12.88	1.54	0.93	1.04	2.20	-0.63	0.83
def2-TZVPD	12.72	12.83	15.84	-12.72	1.67	1.05	1.20	3.07	-0.45	1.12
aug-cc-pVTZ	13.13	13.21	15.86	-13.13	1.46	1.09	1.19	1.80	-1.06	0.55
					BHandHLYP					
6-311+G(d,p)	1.92	2.06	3.87	-1.87	0.88	1.03	1.17	2.57	0.97	0.65
def2-TZVPD	1.90	2.04	3.89	-1.74	1.08	1.22	1.55	4.92	1.15	1.05
aug-cc-pVTZ	2.06	2.16	3.85	-2.06	0.65	0.73	0.82	1.62	0.65	0.51
					HF					
6-311+G(d,p)	15.27	15.73	21.45	15.27	3.78	4.02	4.30	6.11	3.90	1.82
def2-TZVPD	15.29	15.75	21.28	15.29	3.78	4.10	4.50	8.66	3.97	2.11
aug-cc-pVTZ	15.08	15.52	21.25	15.08	3.67	3.78	4.09	5.93	3.65	1.84
					HSE06					
6-311+G(d,p)	11.33	11.40	13.72	−11.33	1.23	0.54	0.70	2.21	-0.20	0.67
def2-TZVPD	11.18	11.27	13.73	−11.18	1.39	0.68	1.03	3.63	-0.02	1.03
aug-cc-pVTZ	11.56	11.61	13.72	−11.56	1.11	0.64	0.71	1.16	-0.60	0.38
					LC-ωPBE					
6-311+G(d,p)	18.77	18.93	23.25	−18.77	2.47	0.57	0.72	2.19	-0.16	0.71
def2-TZVPD	18.57	18.76	23.17	−18.57	2.60	0.73	1.03	3.43	0.03	1.03
aug-cc-pVTZ	18.90	19.05	23.17	−18.90	2.40	0.60	0.71	1.48	-0.53	0.48

[a]Mean absolute error (Mean AE), root mean square (RMS) error, maximum absolute error (Max AE), mean signed error (MSE), and the standard deviation of the error are compared to experimental results.[63,64,65,66,67,68,69] For the shifted errors, the entire spectrum is shifted so that the lowest energy transition matches with experiment and the errors of all the other peaks are evaluated.

Table 4.2.2: Errors for All K-Edge Transitions, Focusing on the Effect of Core & Diffuse Functions

	K-edge Transition Data (eV)[a]									
Basis Set	Absolute Errors					Shifted Errors				
	Mean AE	RMS	Max AE	MSE	Std Dev	Mean AE	RMS	Max AE	MSE	Std Dev
					BP86					
aug-cc-pVTZ	20.45	20.59	24.79	-20.45	2.40	1.98	2.18	3.12	-1.97	0.94
aug-cc-pCVTZ	20.50	20.64	24.88	-20.50	2.42	1.97	2.18	3.12	-1.97	0.93
d-aug-cc-pVTZ	20.96	21.12	25.75	-20.96	2.60	2.68	2.83	4.09	-2.68	0.93
d-aug-cc-pCVTZ	21.01	21.18	25.87	-21.01	2.63	2.69	2.85	4.08	-2.69	0.94
					PBE1PBE					
aug-cc-pVTZ	11.60	11.65	13.80	-11.60	1.12	0.70	0.78	1.26	-0.67	0.40
aug-cc-pCVTZ	11.64	11.70	13.88	-11.64	1.14	0.70	0.78	1.26	-0.67	0.40
d-aug-cc-pVTZ	11.86	11.93	14.43	-11.86	1.25	1.04	1.14	1.77	-1.04	0.48
d-aug-cc-pCVTZ	11.91	11.98	14.52	-11.91	1.27	1.05	1.15	1.78	-1.05	0.48
					B3LYP					
aug-cc-pVTZ	13.13	13.21	15.86	-13.13	1.46	1.09	1.19	1.80	-1.06	0.55
aug-cc-pCVTZ	13.16	13.25	15.93	-13.16	1.48	1.09	1.19	1.79	-1.06	0.55
d-aug-cc-pVTZ	13.42	13.52	16.49	-13.42	1.60	1.48	1.57	2.32	-1.48	0.54
d-aug-cc-pCVTZ	13.46	13.56	16.57	-13.46	1.62	1.49	1.58	2.32	-1.49	0.55
					BHandHLYP					
aug-cc-pVTZ	2.06	2.16	3.85	-2.06	0.65	0.73	0.82	1.62	0.65	0.51
aug-cc-pCVTZ	2.09	2.19	3.87	-2.09	0.65	0.73	0.82	1.61	0.65	0.51
d-aug-cc-pVTZ	2.22	2.31	3.85	-2.22	0.62	0.57	0.68	1.50	0.42	0.53
d-aug-cc-pCVTZ	2.25	2.34	3.87	-2.25	0.62	0.57	0.68	1.51	0.42	0.54
					HF					
aug-cc-pVTZ	15.08	15.52	21.25	15.08	3.67	3.78	4.09	5.93	3.65	1.84
aug-cc-pCVTZ	15.05	15.49	21.22	15.05	3.66	3.78	4.09	5.95	3.65	1.84
d-aug-cc-pVTZ	15.01	15.44	21.15	15.01	3.62	3.67	4.00	5.85	3.55	1.84
d-aug-cc-pCVTZ	14.98	15.41	21.12	14.98	3.61	3.68	4.01	5.87	3.55	1.85
					HSE06					
aug-cc-pVTZ	11.56	11.61	13.72	-11.56	1.11	0.64	0.71	1.16	-0.60	0.38
aug-cc-pCVTZ	11.59	11.65	13.79	-11.59	1.13	0.64	0.71	1.15	-0.60	0.38
d-aug-cc-pVTZ	11.84	11.90	14.32	-11.84	1.24	1.00	1.09	1.64	-1.00	0.42
d-aug-cc-pCVTZ	11.88	11.95	14.41	-11.88	1.26	1.01	1.10	1.66	-1.01	0.43
					LC-ωPBE					
aug-cc-pVTZ	18.90	19.05	23.17	-18.90	2.40	0.60	0.71	1.48	-0.53	0.48
aug-cc-pCVTZ	18.94	19.10	23.25	-18.94	2.43	0.60	0.71	1.48	-0.53	0.48
d-aug-cc-pVTZ	19.08	19.24	23.36	-19.08	2.46	0.78	0.93	1.66	-0.78	0.51
d-aug-cc-pCVTZ	19.11	19.28	23.43	-19.11	2.49	0.78	0.93	1.65	-0.78	0.51

[a]Mean absolute error (Mean AE), root mean square (RMS) error, maximum absolute error (Max AE), mean signed error (MSE), and the standard deviation of the error are compared to experimental results.[63,64,65,66,67,68,69] For the shifted errors, the entire spectrum is shifted so that the lowest energy transition matches with experiment and the errors of all the other peaks are evaluated.

Time and space are modes by which we think and not conditions in which we live.

Albert Einstein

5

Time-Dependent Polarizable Continuum

5.1 Introduction

The group of processes conjointly known as charge transfer (CT) is among the most fundamental and important in all disciplines of chemistry, as well as physics and biology.[13] The multitude of reactions driven by CT, ranging from photosynthesis to ATP conversion and photovoltaics, has put it at the forefront of scientific research for the past several decades and more to come. In recent years, due to its direct photovoltaic applications, ultrafast photo-induced intramolecular CT has been propelled into the limelight of energy and semiconductor research.[14,15,16,17,18,19,20,21] In this special type of CT process, the excitation and electronic response occur typically on the femtosecond timescale. Given how ultrafast photo-induced intramolecular CT epitomizes the general mechanism of CT process, a meticulous elucidation on its dynamics could potentially lead to a wealth of useful information.

In modeling CT, it is of immense interest to reasonably include the effect of solvent, since it

typically involves a highly polar species in solution. The solute's strong permanent dipole actively interacts with the polar solvent, inducing intimate coupling between them. As often is the case when there is an intermolecular charge separation, charge-transfer-prone species are extremely sensitive to the dielectric response of the surrounding solvent, yielding substantial spectral shifts going from non-polar to polar solvent. Such photochemical properties can be in principle computed using any excited state electronic structure method with a solvation model: explicit (using real solvent molecules) or implicit (using polarizable continuum models).

Of particular interest is the dynamics of an excited CT state in solution, where solvation effects can change the fundamental CT process, and drastically modify the transfer rate. However, intricate intertwining of nuclear and electronic degrees of freedom from both solute and solvent renders probing the dynamics of solvated CT processes a challenge to experimentalists and theoreticians alike. In this work, we extend our well-established real-time, time-dependent density functional theory (RT-TDDFT), coupled with a time-dependent polarizable continuum model (TDPCM) that includes a solvent dielectric relaxation approach. We will apply this new method to study the dynamics of the intramolecular excited CT state of *p*-nitroaniline (pNA) in acetonitrile.

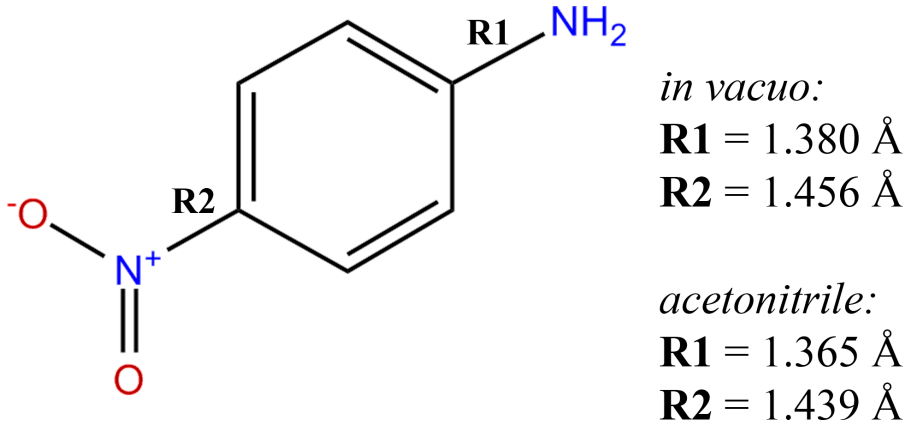

Figure 5.1.1: Molecular structure of ground state pNA.

pNA (fig. 5.1.1) is a classic model molecule for theoretical[73,74,75,76] and experimental[77,78,79] investigations of CT properties. With a donor group (NH_2) linked to an acceptor group (NO_2),

pNA showcases properties associated with the CT process. Also, the large change in pNA's dipole moment ($\Delta\mu = 9.3$ Debye in dioxane[80]) upon photo-excitation renders it quite susceptible to a solvent's polarity, indicative by the 5000 cm^{-1} solvatochromatic shift.[81] Coupled with the relatively small energy difference between the lower excited states,[82] pNA's strong energy dependence on the solvent polarity could potentially change the ordering of the lowest states, leading to varied reaction pathways.

5.2 Methodology

The interaction between solute and solvent is modeled using the PCM method with time-dependent solute electronic density.[83] PCM approximates the solvent as a continuous dielectric medium with an embedded cavity that hosts the solute.[84,85] The solute-solvent interaction is obtained by solving the Poisson equation with the appropriate boundary conditions and is expressed as a quantum mechanical self-consistent reaction field (SCRF). Such a reaction field can be represented by an apparent surface charge (ASC) density placed on the surface cavity. The ASC density can be determined using a variety of methods depending on which model of the PCM family is being implemented. Practical applications of all PCM methods also require a discrete representation of the ASC density over the solute-solvent interface. The integral equation formalism PCM (IEF-PCM)[86,87,88,89] and the continuous surface charge (CSC) formalism[90] are used in this work, but the implementation with RT-TDDFT can be generalized to any discrete charge formalism. In the CSC method, the apparent surface charge density is represented in a basis of spherical Gaussian functions $\{\varphi\}$ with the polarization charges $\{q\}$ as the expansion coefficients. Given the charge distribution defined by such a representation, the PCM reaction potential, V^{PCM} enters the solute Hamiltonian as an instantaneous perturbation at time t,

$$\mathbf{K}(t) = \mathbf{K}_0(t) + \mathbf{V}^{\mathrm{PCM}}(t) \tag{5.1}$$

$$V^{\mathrm{PCM}}_{\mu\nu} = \sum_i \iint \frac{q_i \varphi_i(\mathbf{r}) \chi_\mu(\mathbf{r}') \chi_\nu(\mathbf{r}')}{|\mathbf{r} - \mathbf{r}'|} \, \mathrm{d}^3\,\mathbf{r}\, \mathrm{d}^3\,\mathbf{r}' \tag{5.2}$$

If the electronic density of the solute is expanded in an atomic orbital (AO) basis $\{\chi\}$, its

electrostatic potential V_i acting on the solvent can be expressed as (in atomic units),

$$V_i(t) = \sum_A \int \frac{Z_A \varphi_i(\mathbf{r})}{|\mathbf{r} - \mathbf{R}_A|} \, d^3\,\mathbf{r} - \sum_{\mu\nu} P_{\mu\nu}(t) \iint \frac{\varphi_i(\mathbf{r}) \chi_\mu(\mathbf{r}') \chi_\nu(\mathbf{r}')}{|\mathbf{r} - \mathbf{r}'|} \, d^3\,\mathbf{r}\, d^3\,\mathbf{r}' \tag{5.3}$$

where Z_A and $\mathbf{R}_A$ are solute nuclear charges and positions, and $P_{\mu\nu}$ are matrix elements of the time-dependent electronic density of the solute. With this time-dependent solute electrostatic potential, the equilibrium state of the solvent polarization charges can be obtained by solving the discretized PCM equations self-consistently with a given solvent dielectric permittivity ε (see Refs. 91, 90, 83, 92 for detailed derivations). This approach (eqs. (5.1) to (5.3)) will be referred to as TDPCM throughout this paper. Note previous work on TDPCM,[93,94,95] are related to the response function formalism, while this work is strictly in the time-domain. The combined TDDFT electronic dynamics and TDPCM solvent dynamics is the foundation of the first-principles solvated electronic dynamics presented herein. On one hand, the time-dependent solute electronic density polarizes the PCM charge distribution. On the other, the time-dependent solvent reaction field becomes an instantaneous perturbation to the solute electronic motion.

In TDPCM, the solvent is modeled with a charge density characterized by the dielectric constant, ε, which is directly associated with the discretized ASC $\{q\}$, given a solute reaction potential. There are two kinds of ε considered in this work: the optical ε_∞ is the dynamical contribution associated with the solvent electronic motion, whereas the bulk or static ε_o also includes inertial or orientational contribution, related to its nuclear motion.[96,97] Solvent electronic motion is assumed to equilibrate instantaneously to the solute reaction potential while the response of solvent nuclear degrees of freedom takes place on a longer time-scale. The bulk dielectric constant ε_o is sufficient for computing most thermodynamics or non-optical properties such as heats of reaction and barrier heights. The optical dielectric constant is often used in calculating vertical electronic excitations. However, when the solute electronic dynamics following a photo-excitation is on the same time-scale of the solvent dielectric relaxation from optical to bulk, representing the solvent by a single dielectric constant, either optical or bulk, is obviously nonphysical, especially when the solute net dipole change $\Delta\mu$ is significant.[98]

In this work, we propose a relaxation model to account for the time-dependent solvent

response transitioning from optical to bulk dielectric. Upon photo-excitation of the solute, the solvent's instantaneous response to the solute reaction potential takes on the optical dielectric constant, ε_∞. As the solvated electronic dynamics proceeds, the solvent nuclear degrees of freedom start to contribute to the solvent response, and therefore the dielectric constant will gradually represent the bath-like behavior of the bulk medium, ε_0. Such time-dependent solvent relaxation is modeled with eq. (5.9), that satisfies the boundary conditions, $\varepsilon(0) = \varepsilon_\infty$ and $\lim_{t\to\infty} \varepsilon(t) = \varepsilon_0$.

Following the notations and derivations used in Refs. 91 and 99, we start with a working equation that relates PCM polarization charges q to the electric field generated by the solute,

$$\left(2\pi\frac{\varepsilon_0 + 1}{\varepsilon_0 - 1}\mathbf{A}^{-1} - \mathbf{D}^*\right)\mathbf{q} = -\mathbf{E}_\perp \tag{5.4}$$

where $\mathbf{D}^*$ accounts for the electric field generated by $\{q\}$ (see Ref. 99 for complete definition of $\mathbf{D}$), and $\mathbf{E}_\perp$ are the normal components of the electric field generated by the solute on the cavity surface. $\mathbf{A}$ represents the small areas $\{a\}$ on the cavity surface where $\{q\}$ are centered. Solving eq. (5.4) iteratively, we then have:

$$q_i^{(n)} = \left\{\frac{1}{a_i}\left[\frac{4\pi\varepsilon_0}{\varepsilon_0 - 1} + z_i(a_j)\right]\right\}^{-1}\left\{-(E_\perp)_i + z_i^*\left[q_j^{(n-1)}\right]\right\} \tag{5.5}$$

where $z_i(a_j) = \sum_{j\neq i} D_{ij}a_j$ and $z_j^*(q_j) = \sum_{j\neq i} D_{ij}^* q_j$. As the polarization charge q_i serves as the primary link between solvent and solute, we need to determine the dynamic response of q_i. **(author?)** [91] defined the variation of q_i at time t as a response to the change in the electric field:

$$\delta q_i^{(n)}[(\Delta E_\perp)_i, t] = g_i(t)\left\{-(\Delta E_\perp)_i + z_i^*\left[\delta q_j^{n-1}\right]\right\} - \frac{z_i[a_j]}{a_i}\delta q_i^{n-1} \tag{5.6}$$

Assuming the Debye model for the solvent relaxation, the time-dependent function $g_i(t)$ in eq. (5.6) can be approximated as:[91]

$$g_i^\star(t) \simeq -\frac{a_i}{4\pi\varepsilon_0}\left(\frac{\Delta\varepsilon}{\varepsilon_\infty}e^{-Bt} + \varepsilon_0 - 1\right) \tag{5.7}$$

where $\Delta\varepsilon = \varepsilon_0 - \varepsilon_\infty$, $B = \frac{1}{\tau'}\frac{\varepsilon_0}{\varepsilon_\infty}$ and τ' is the solvent response time.

Since the solvent response can be approximated with a simple relaxation from being optically active to static, we propose an alternative to eq. (5.7) by assimilating all the time-dependency of $g(t)$ into the dielectric term ε in eq. (5.4). Such a function can be constructed by comparing eqs. (5.5) and (5.6), and we get:

$$g_i^{\star\star}(t) \simeq \left[\frac{1}{a_i}\left(\frac{4\pi\varepsilon(t)}{\varepsilon(t)-1}\right)\right]^{-1} \tag{5.8}$$

In this expression, we introduce a time-dependent dielectric term $\varepsilon(t)$. Equations (5.7) and (5.8) are both approximations of the same physical behavior. By equating these two equations, the PCM charge cavity representation a_i can be completely eliminated, so is the dependency on any specific PCM formulation. Finally we have:

$$\varepsilon(t) = \frac{\varepsilon_0 \cdot \varepsilon_\infty}{\varepsilon_\infty + \Delta\varepsilon \cdot e^{-Bt}} \tag{5.9}$$

$$B = \frac{1}{\tau'}\frac{\varepsilon_0}{\varepsilon_\infty} \tag{5.10}$$

$$\tau' = \tau_D \frac{\varepsilon_\infty}{\varepsilon_0} \tag{5.11}$$

where τ_D is the solvent Debye relaxation time and $\Delta\varepsilon = \varepsilon_0 - \varepsilon_\infty$. τ' is also known as the time-constant of the response function of solvent reaction field.[98,95,100] At every time step, ε will be updated according to eq. (5.9) together with the RT-TDDFT and TDPCM. An example of the solvent dielectric relaxation profile modeled by eq. (5.9) is illustrated in fig. 5.2.1 and will be discussed with computational example in the next section. Note when a different PCM model is used, simple revision of this derivation will still generate the same time-dependent dielectric relaxation model. For example, using eq. (5.8) without the tesserae area a_i with the IEF-PCM formulation[95] will result in the exact same expression for $\varepsilon(t)$.

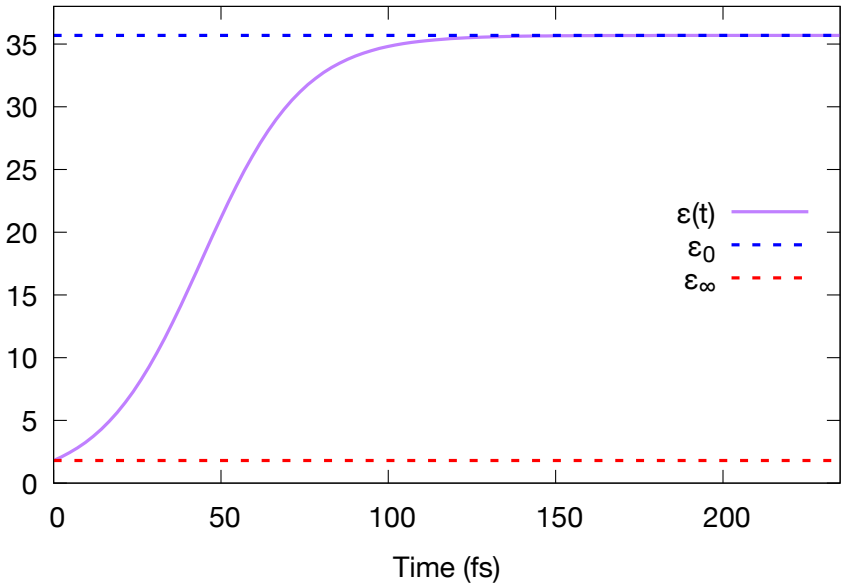

Figure 5.2.1: Time-dependence of the dielectric for acetonitrile according to eq. (5.9) with $\tau_D = 5.9$ ps, $\varepsilon_o = 35.7$, and $\varepsilon_\infty = 1.8$

5.3 Result and Discussion

All calculations were carried out using the development version of the Gaussian software suite[30] with the addition of RT-TDDFT and TDPCM algorithms with solvent relaxation model introduced in this work. The B3LYP exchange-correlation functional[27,28,29] along with 6-31G(d) basis set were used for geometry optimizations, linear response calculations, and solvated electronic dynamics. The ground state of the pNA molecule was fully optimized in both vacuum and acetonitrile PCM. The ground state equilibrium geometries obtained for both cases are very similar with a few minor differences indicated on fig. 5.1.1. This is expected as the compactness of the structure and the stabilizing effect of the benzene ring don't allow for much deviation.[101] Along with the structural changes, the molecular dipole moment of the ground state of pNA increases from 7.12 Debye (exp. 6.87 Debye[76]) in vacuum to 9.95 Debye in acetonitrile.

Table 5.3.1 lists the lowest three vertical excitation energies and characteristics of these excited states, calculated using the linear response formalism of TDDFT.[103,104,105,106] Excitations for

Table 5.3.1: Calculated absorption spectrum and excited states properties of pNA.

Excited state	Dominant transition	Excitation energy (eV)	Oscillator strength	Dipole (Debye)
		in vacuo		
1	HOMO - 2 → LUMO	3.8 [a]	0.0000	4.9
2	HOMO → LUMO	4.1	0.3223	12.2
3	HOMO - 3 → LUMO	4.4	0.0001	5.2
		acetonitrile		
1	HOMO → LUMO	3.5 [b]	0.5720	15.8
2	HOMO - 2 → LUMO	3.8	0.0000	7.0
3	HOMO - 1 → LUMO HOMO → LUMO+1	4.4	0.0054	14.9

[a] Exp: 4.24;[97] [b] Exp: 3.41[97,102]

pNA in acetonitrile are computed using the optical dielectric constant ε_∞ of the solvent. Among the lower lying excitations in the vacuum, only the second lowest excited state is transition-dipole allowed. This state is associated with the electronic transition from the highest occupied molecular orbital (HOMO) to the lowest unoccupied molecular orbital (LUMO) (fig. 5.3.1), which leads to an increase of the overall dipole moment by $\sim$ 5.1 Debye. In contrast, vertical excitations of pNA in acetonitrile show slightly different characteristics. The lowest excitation is now the HOMO-LUMO transition with a larger transition dipole moment, a net dipole increase of $\sim$ 5.9 Debye and a red-shift of the excitation energy of $\sim$ 0.6 eV. These observations are well-known results of polar solvent introduced stabilization of CT states, and are in very good agreement with the equation-of-motion coupled cluster results of Kosenkov and Slipchenko,[107] and molecular dynamics simulation by Moran *et at.*[108] Static calculations, such as those listed in table 5.3.1, are informative about reaction energetics and photochemical properties. However, studies of other important dynamical properties, such as solvent response and the lifetime of CT state upon solvent perturbation, require dynamical simulations, presented in the following sections.

Our real time solvated electronic dynamics start with the photo-excited CT states found via the linear response calculations. For the vacuum case, the initial CT state is the second lowest

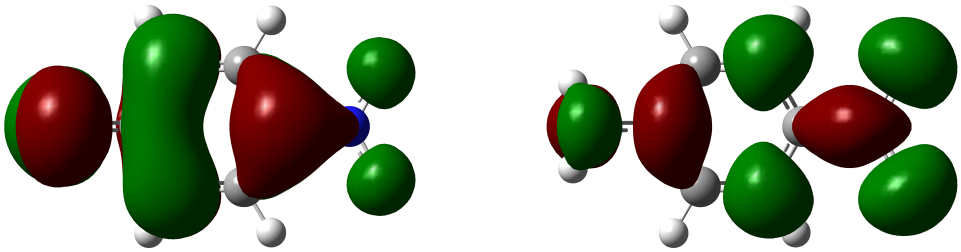

Figure 5.3.1: Molecular orbitals for for HOMO (left) and LUMO (right).

excited state whereas it is the lowest excited state of pNA in acetonitrile. The initial electronic density is prepared by promoting one electron from HOMO to LUMO as suggested by the linear response calculations in table 5.3.1. Starting with the photo-excited CT state, solvated dynamics is simulated using the RT-TDDFT method with TDPCM with solvent dielectric relaxation model, introduced above. The solute dynamics presented in this work addresses pure electronic relaxation because ultrafast dynamics ($\sim$100 fs) is usually dominated by the electronic degrees of freedom. To analyze the electronic dynamics and compare it to linear response calculations, the time-dependent density is projected on the ground state orbital space:

$$n_k(t_i) = \mathbf{C}_k^\dagger(0)\mathbf{P}(t_i)\mathbf{C}_k(0) \tag{5.12}$$

where $\mathbf{C}_k(0)$ is the k^{th} eigenvector of the initial ($t = 0$) Kohn-Sham matrix.[11] The time-dependent dipole moment, $\mu(t)$, is computed using the time-dependent electronic density,

$$\mu_{\{x,y,z\}}(t) = \sum_a Z_a R_{a,\{x,y,z\}} - \mathrm{Tr}[\mathbf{d}_{\{x,y,z\}} \cdot \mathbf{P}(t)] \tag{5.13}$$

where Z_a and $R_{a,\{x,y,z\}}$ are the nuclear charge and coordinates of the a^{th} atom, and $\mathbf{d}_{\{x,y,z\}}$ is the dipole matrix. We use the isotropic time-dependent dipole, $\bar{\mu}(t) = \sqrt{\mu_x^2(t) + \mu_y^2(t) + \mu_z^2(t)}$, in the following analysis.

Figures 5.3.2a and 5.3.2b show the time-evolution of the photoexcited electron/hole and solute dipole moment in vacuum. The electronic dynamics shows that the CT excited state

quickly relaxes to the ground state within ∼10 fs via coherent LUMO→HOMO transition. Because there is no energy dissipation for the solute electronic degrees of freedom in vacuum, coherent oscillation continues after the initial relaxation. The time-dependent dipole (fig. 5.3.2b) suggests that the LUMO → HOMO transition is associated with back CT that leads to a reduction of the net dipole moment from ∼12 to ∼7 Debye, in good agreement with the prediction from linear response calculations. The oscillations in the orbital occupation numbers die down after about 50 fs. To model the solvent relaxation, we use the experimental Debye relaxation constant for acetonitrile $\tau_D = 5.9$ ps.[100] The time-dependent solvent dielectric constant, plotted in fig. 5.2.1 using eq. (5.9), shows the increase of the effective solvent dielectric constant, starting with $\varepsilon_\infty = 1.8$ Debye at $t = 0$ and approaching the bulk value of 35.7 Debye near 150 fs. Table 5.3.1 suggests that the static electronic characteristics of excited states in solvent is rather different from those in vacuum. As shown in figs. 5.3.3a and 5.3.3b, the electronic dynamics of pNA in acetonitrile also exhibits very different physical chemistry compared to those in figs. 5.3.2a and 5.3.2b. The solute excited CT state is stabilized by the acetonitrile, showing a much longer lifetime (∼10 fs → ∼140 fs). In the propagation scheme developed in this work, the PCM charge distributions are brought to self-consistency to the time-dependent solute electrostatic potential described in eq. (5.3). In other words, the solvent charge distribution is in instantaneous equilibrium with the time-dependent solvent potential. This procedure can be considered as the PCM *dissipates* excessive energy with the solvent acting as a thermal bath when the solute gradually relaxes from the excited CT state to the ground state. As a result, the coherent oscillation seen in the vacuum case is absent in fig. 5.3.3a. Accompanied with the LUMO → HOMO transition, the solute dipole moment decreases from ∼19 Debye of the excited CT state to ∼10 Debye of the ground state. The CT lifetime of pNA in acetonitrile was found to be 140 fs, in good agreement with experimental observations using the transient absorption spectra by Kovalenko *et al.*[102]

In order to illustrate the importance of solvent dielectric relaxation on the CT lifetime, we have carried out simulations without time-dependent dielectric model, and instead using a fixed optical or bulk dielectric constant. These simulations show a much longer lifetime (>500 fs) of excited state CT state of the solute. In a separate set of simulations, we tested the effect of Debye relaxation time of a solvent on the CT process of the solute. We have carried out multiple

simulations using the solvent dielectric relaxation model introduced here with $\tau_D \in [0.1, 100]$ ps. We noticed that when τ_D is too small (e.g. $\sim$ 0.1 ps) or too large ($\sim$ 100 ps), the solvent dielectric property can be considered constant during the lifetime of the excited CT state. In this case, the excited CT state is "over-stabilized", i.e. with a lifetime that is much longer than experimental observation. These observations suggest that the solvent dielectric relaxation is a crucial perturbation that leads to the relaxation of excited solute CT state.

5.4 Conclusion

In this work, we introduced a TDPCM method with a dielectric relaxation model to simulate solvated first-principles electronic dynamics. We posit that the complex solvent response can be adequately approximated with two processes. First, the direct interaction between solvent and solute is explicitly described and propagated in time by coupling the solvent reaction field to the time-dependent electronic density of solute. Second, as the solute relaxes from being vertically excited, the solvent also undergoes its own relaxation, from being optically active to a bath-like bulk medium, modeled by a dielectric relaxation model introduced in this paper. This time-dependent solvation model with RT-TDDFT satisfactorily demonstrates the effects of solvent on the CT process, yielding consistent results, i.e. CT lifetime, with expectation based on experimental data.

Note that a better yet much more difficult approach is to propagate the solvent charge distribution in the time-domain instead of solving the PCM equation to self-consistency at every time step. In light of the recent development of a variational PCM method,[109] a complete solvent-solute dynamics can be propagated on the same footing. In other words, the subtle retardation of the solvent response can be addressed in near future.

This method holds the potential to model a broad range of excited state dynamics in solvent. For instance, the prediction of a CT process lifetime in different solvents is crucial to the establishment of excitons in solar energy harvesting and storage. Also, the solvent-specific reorganization of electronic states can potentially open up reaction pathways that are inaccessible in gas phase or other solvents. An accurate description of the solvated excited state chemical dynamics afforded by this tool would offer important insights into the dynamical interplay between solvent and solute.

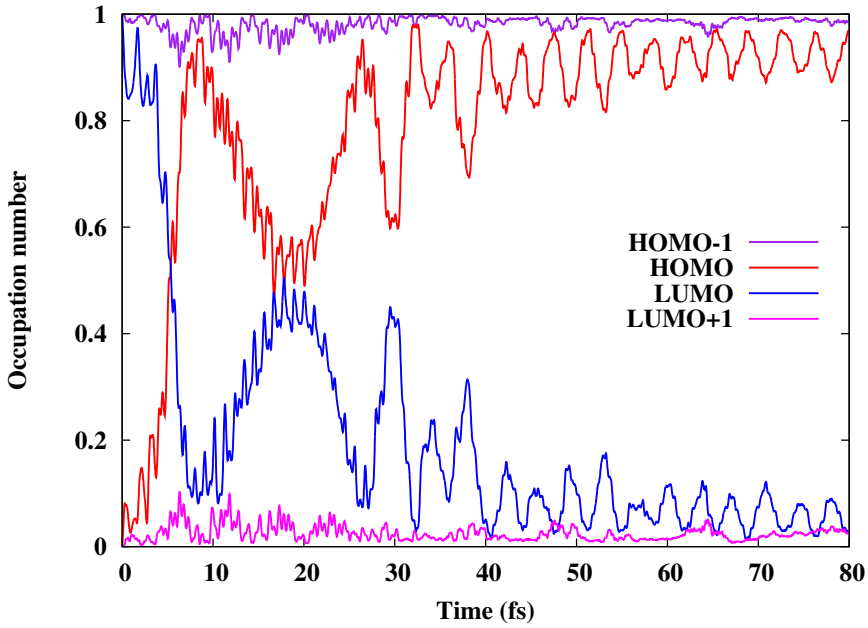

(a)

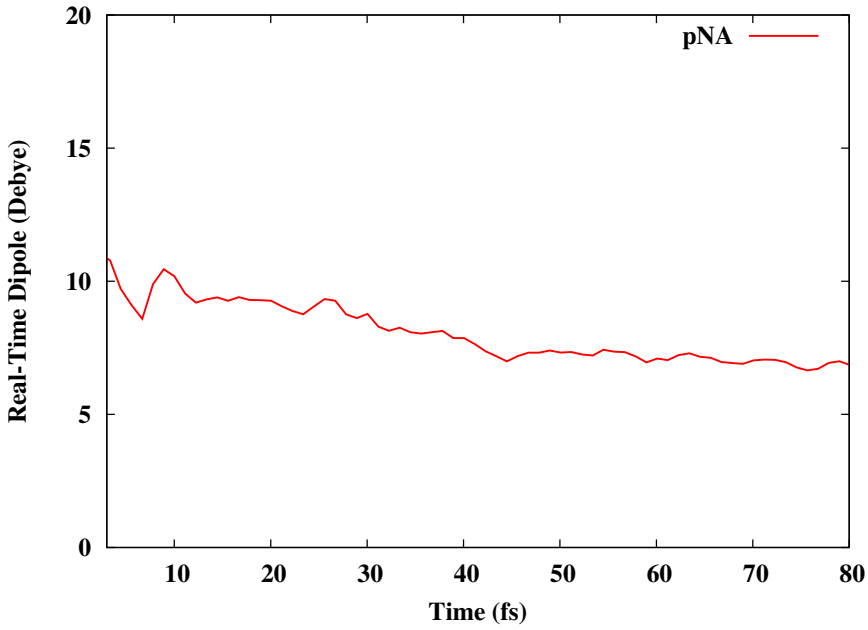

(b)

Figure 5.3.2: Time evolution of the photoexcited pNA following the HOMO→LUMO excitation at time $t = 0$ in vacuum. (a) Time-dependent electronic density projected on the ground state molecular orbital space computed at $t = 0$. (b) Time-dependent isotropic dipole moment.

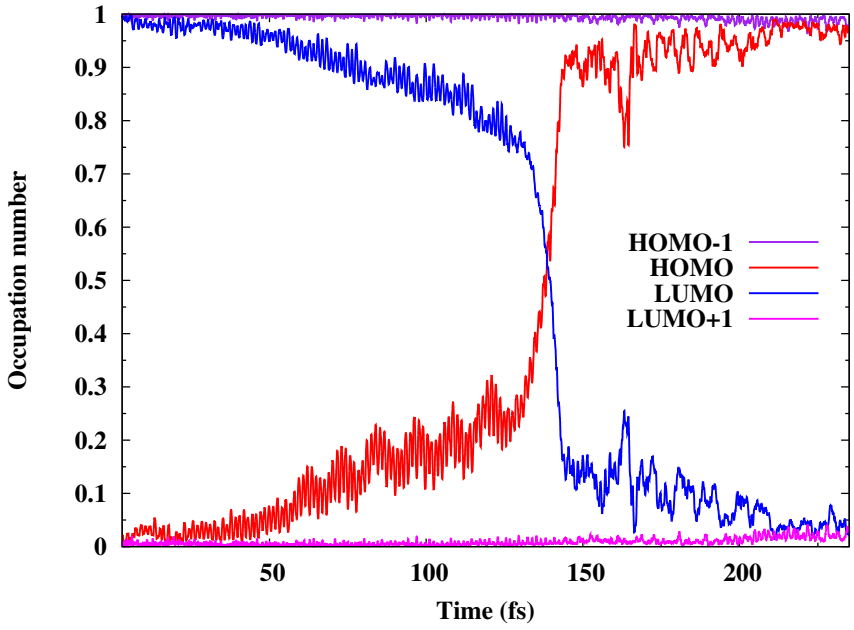

Figure 5.3.3: Time evolution of the photoexcited pNA following the HOMO→LUMO excitation at time $t = 0$ in acetonitrile. (a) Time-dependent electronic density projected on the ground state molecular orbital space computed at $t = 0$. (b) Time-dependent isotropic dipole moment.

6

Chebyshev Expansion

Having demonstrated the importance of the time-dependence perturbation potential in the Hamiltonian, we shall now focus on the other aspect of the time-dependent method: the propagation of the electronic density in time, i.e. evaluating the time evolution operator $\hat{\mathbf{U}}$ from **??**, There are numerous methods to evaluate $\hat{\mathbf{U}}$, such as numerical integration like Runge-Kutta, the split-operator method or the direct evaluation of the exponential function like MMUT. As shown in **??** and eq. (2.59), MMUT requires direct diagonalization of the Hamiltonian/Kohn-Sham matrix. Our recent interest in photovoltaic devices necessitates the dynamic simulations of large systems such as organic solar cell polymers and quantum dots. However, the sheer size of these systems has drastically increased the cost of using RT-TDDFT, prompting us to look for alternatives. Formally scaling as $\mathcal{O}(N^3)$ where N is the number of basis functions, matrix diagonalization is the obvious limiting factor besides the computation of the Hamiltonian itself. We propose an alternative to the MMUT step in RT TD-DFT that avoid

matrix diagonalization completely by a polynomial expansion of the time-evolution operator $\hat{\mathbf{U}}$.

$$\Psi(t) = \exp\left(-i\hat{\mathbf{H}}t\right)\Psi(0) = \sum_n a_n P_n(\hat{\mathbf{H}})\Psi(0) \tag{6.1}$$

Polynomials methods can be divided into two groups: those that choose the type of polynomial in advance (Newton, Chebyshev, Fabor) and those that do not (the Short Iterative Lanczos/Arnoldi scheme using the Krylov space). Chebyshev polynomials have been shown[?] to have high numerical stability and accuracy while being efficient with memory.[?,?] The rest of this paper will present the framework for how to propagate a TD-DFT electronic density in time using the Chebyshev polynomial expansion scheme.

We first start with the more generalized version of **??**:

$$\mathbf{P}(t+\Delta t) = \exp\left(-i[\mathbf{K}(t), \mathbf{P}(t)]\Delta t\right) \cdot \mathbf{P}(t) \tag{6.2}$$

$$= \underbrace{\exp\left(-i\mathbf{K}(t)\Delta t\right)}_{\hat{\mathbf{U}}} \cdot \mathbf{P}(t) \cdot \underbrace{\exp\left(i\mathbf{K}(t)\Delta t\right)}_{\hat{\mathbf{U}}^\dagger} \tag{6.3}$$

given a Δt small enough so that $\mathbf{K}$ can be assumed to remain constant. Using the complex version of Chebyshev polynomials of the first kind, which are defined as:

$$\varphi_n(\omega) = i^n T_n(\omega), \qquad \omega \in [-i, i] \tag{6.4}$$

The generating equations for Chebyshev polynomials are:

$$\begin{aligned} \varphi_0(\omega) &= 1 \\ \varphi_1(\omega) &= \omega \\ \varphi_{n+1}(\omega) &= 2\omega\varphi_n(\omega) + \varphi_{n-1}(\omega) \end{aligned} \tag{6.5}$$

Any exponential function such as $\hat{\mathbf{U}}$ can thus be expanded as:

$$\exp(-ia x) = \sum a_n(a)\varphi_n(-ix) \tag{6.6}$$

$$a_n(a) = \int_{-i}^{i} \frac{\exp(iax)\varphi_n(x)}{\sqrt{1-x^2}} dx = \begin{cases} J_0(a), & n = 0 \\ 2J_n(a), & n > 0 \end{cases} \tag{6.7}$$

$$J_n(a) = \sum_{m=0}^{\infty} \frac{(-1)^m}{m!(m+n)!} \left(\frac{a}{2}\right)^{2m+n}, \qquad n \geq 0 \tag{6.8}$$

where $J_n(a)$ are the Bessel functions of the first kind as defined in eq. (6.8). Before expanding the first exponential term in eq. (6.3), the values of $-i\mathbf{K}$ have to be mapped onto the domain of the Chebyshev polynomials $[-i, i]$:

$$\mathbb{K} = \frac{\mathbf{K} - \Delta E/2 + E_{min}}{\Delta E/2} \tag{6.9}$$

$$\Rightarrow \mathbf{K} = \frac{\mathbb{K}\Delta E}{2} + \frac{\Delta E}{2} + E_{min} \tag{6.10}$$

where $\Delta E = 2(E_{max} - E_{min})$ is the twice the range of eigenvalues of $\mathbf{K}$, i.e. the MO energies which can be extract from the ground state static molecule. The range of MO energies has been doubled to ensure that the expanded function doesn't misbehave during the course of the dynamics. We can now generate the Chebyshev polynomials iteratively and obtain the full expansion of $\hat{\mathbf{U}}$ as:

$$\begin{aligned} \varphi_0 &= 1 \\ \varphi_1 &= -i\mathbb{K} \\ &\vdots \\ \varphi_n &= -2i\mathbb{K}\varphi_{n-1}(-i\mathbb{K}) + \varphi_{n-2}(-i\mathbb{K}) \end{aligned}$$

$$\exp\left(-i\mathbf{K}\Delta t\right) = \exp\left[-i\left(a + E_{min}\right)\Delta t\right]\left[\sum a_n(a)\varphi_n(-i\mathbf{K})\right] \tag{6.11}$$

where $a = \dfrac{\Delta E \cdot \Delta t}{2}$. The matrix obtained from eq. (6.11) is the fully expanded $\hat{\mathbf{U}}$, from which the complex conjugate $\hat{\mathbf{U}}^\dagger$ can be trivially computed. Finally, we can assemble everything: $\hat{\mathbf{U}}$, $\hat{\mathbf{U}}^\dagger$ and

$\mathbf{P}(t)$ as in eq. (6.3) to arrive at the electronic density matrix $\mathbf{P}(t + \Delta t)$ propagated over a small time step Δt.

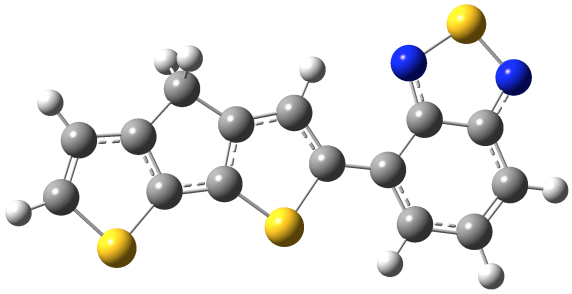

Figure 6.0.1: Ground state structure of the PCPDTBT monomer unit used in benchmark calculation. Yellow spheres represent sulfur atoms

Each iteration of the Chebyshev polynomial only requires the storage of the two immediately previous terms, so the memory footprint of the propagation remains constant for the entire procedure. Also, each iteration requires at most one matrix-matrix multiplication and one matrix-matrix addition, so the total number of matrix operations depends linearly on n - the number of iterations, which is arbitrarily fixed at 20 in the current implementation. The initial benchmark results of the Chebyshev propagator are very encouraging. table 6.0.1 compares the total running time of 100-step RT-TDDFT simulations using MMUT scheme against those using the Chebyshev for pNA, fullerene, and PCPDTBT – an organic polymer used in solar cells whose single unit structure is shown in fig. 6.0.1. The systems were propagated at two different time steps, 0.05 and 0.1 au. At the smaller time step, both schemes of propagation converse the system energy up to 10^{-6} – 10^{-7} Hartrees. The energy conservation slightly degraded to 10^{-5} – 10^{-6} when switching to the larger time with MMUT, yet remained steady at 10^{-6} if Chebyshev was used. All simulations were done on a workstation using 8 cores out of 16 from the Intel Xeon E5-2660 processor. The current implementation of the Chebyshev scheme is still at very early stage, with plenty of bugs and issues remained. For instance, rather than fixing the number of iteration at 20, it would be more efficient if the expansion stops when the difference between two successive iterations gets below a certain threshold. The main appeal of the Chebyshev method is

Table 6.0.1: Preliminary benchmark results comparing running times of MMUT and Chebyshev propagation schemes.

System	Basis fuctions	MMUT (s)	Chebyshev (s)
	$\Delta t = 0.05$ au		
pNA	162	42	38
PCPDTBT monomer	366	621	593
C_{60}	540	2101	1913
PCPDTBT dimer	728	4561	4178
	$\Delta t = 0.1$ au		
pNA	162	25	20
PCPDTBT monomer	366	323	295
C_{60}	540	978	814
PCPDTBT dimer	728	1923	1785

contingent on how well a finite set of simple matrix operations performs compared to another much more complex matrix operation. Although the running time of *N*x*N* square matrices multiplication also formally scales as $\mathcal{O}(N^3)$, extensive works have been done to fine-tune the procedure. Ready-to-use, free and commercial math libraries such as BLAS or Intel MKL are already performing matrix multiplication with optimized algorithms while also taking advantage of modern parallel computing hardware. Advances in technology such as general-purposed GPU will only make matrix-matrix multiplication even more efficient. The molecules used in this benchmark are still relatively small so we are actively working to improve the code and run more tests on much larger systems (2000 basis functions more more). The results shown here are more than enough proofs that Chebyshev propagation is a solid concept and deserves further investigation.

References

[1] Ryan C. Nelson and Jeffrey T. Miller. An introduction to x-ray absorption spectroscopy and its in situ application to organometallic compounds and homogeneous catalysts. *Catal. Sci. Technol.*, 2:461–470, 2012.

[2] Erwin Schrödinger. An Undulatory Theory of the Mechanics of Atoms and Molecules. *Am. Physik*, 79:361, 1926.

[3] Phu D. Nguyen, Feizhi Ding, Sean A. Fischer, Wenkel Liang, and Xiaosong Li. Solvated first-principles excited state charge transfer dynamics with time-dependent polarizable continuum model and solvent dielectric relaxation. *J. Phys. Chem. Lett.*, 3:2898–2904, 2012.

[4] Matthew Gliboff, Dana Sulas, Dennis Nordlund, Dane W. deQuilettes, Phu D. Nguyen, Gerald T. Seidler, Xiaosong Li, and David S. Ginger. Direct measurement of acceptor group localization on donor–acceptor polymers using resonant auger spectroscopy. *J. Phys. Chem. C*, 118:5570–5578, 2014.

[5] Chang-Zhi Li, Po-Wei Liang, Dana B Sulas, Phu D. Nguyen, Xiaosong Li, David S Ginger, Cody W Schlenker, and Alex K.-Y. Jen. Modulation of Hybrid Organic–Perovskite Photovoltaic Performance by Controlling the Excited Dynamics of Fullerenes. *Mater. Horiz.*, 2:414–419, 2015.

[6] Patrick J Lestrange, Phu D. Nguyen, and Xiaosong Li. Calibration of Energy-Specific TDDFT for Modeling K-edge XAS Spectra of Light Elements. *J. Chem. Theor. Comput.*, 11(7):2994–2999, 2015.

[7] J. C. Slater. The theory of complex spectra. *Phys. Rev.*, 34:1293–1322, Nov 1929.

[8] P. Hohenberg and W. Kohn. Inhomogeneous electron gas. *Phys. Rev.*, 136:B864, 1964.

[9] W. Kohn and L. J. Sham. Self-consistent equations including exchange and correlation effects. *Phys. Rev.*, 140:A1133, 1965.

[10] W. Magnus. On the exponential solution of differential equations for a linear operator. *Pure Appl. Math.*, 7:649, 1954.

[11] Xiaosong Li, Stanley M. Smith, Alexei N. Markevitch, Dmitri A. Romanov, Robert J. Levis, and H. Bernhard Schlegel. A time-dependent Hartree-Fock approach for studying the electronic optical response of molecules in intense fields. *Phys. Chem. Chem. Phys.*, 7:233–239, 2005.

[12] Christine M. Isborn, Xiaosong Li, and John C. Tully. "tddft ehrenfest dynamics: Collisions between atomic oxygen and graphite clusters". *J. Chem. Phys.*, 126:134307, 2007.

[13] K.V. Mikkelsen and Mark A Ratner. Electron Tunneling in Solid-state Electron-transfer Reactions. *Chem. Rev.*, 87(1):113–153, 1987.

[14] G. Yu and A. J. Heeger. Charge separation and photovoltaic conversion in polymer composites with internal donor/acceptor heterojunctions. *J. Appl. Phys.*, 78(7):4510 –4515, oct 1995.

[15] Julie M. Rehm, George L. McLendon, Yutaka Nagasawa, Keitaro Yoshihara, Jacques Moser, and Grätzel Michael. Femtosecond electron-transfer dynamics at a sensitizing dye-semiconductor (tio_2) interface. *J. Phys. Chem.*, 100(23):9577–9578, 1996.

[16] I.B. Martini, B. Ma, T. Da Ros, R. Helgeson, F. Wudl, and B.J. Schwartz. Ultrafast competition between energy and charge transfer in a functionalized electron donor/fullerene derivative. *Chem. Phys. Lett.*, 327(5):253–262, 2000.

[17] Alvin T. Yeh, Charles V. Shank, and James K. McCusker. Electron localization dynamics following photo-induced charge transfer. *Science*, 289(5481):935–938, 2000.

[18] David M. Adams, Louis Brus, Christopher E. D. Chidsey, Stephen Creager, Carol Creutz, Cherie R. Kagan, Prashant V. Kamat, Marya Lieberman, Stuart Lindsay, Rudolph A. Marcus, Robert M. Metzger, M. E. Michel-Beyerle, John R. Miller, Marshall D. Newton, Debra R. Rolison, Otto Sankey, Kirk S. Schanze, James Yardley, and Xiaoyang Zhu. Charge transfer on the nanoscale: Current status. *J. Phys. Chem. B*, 107(28):6668–6697, 2003.

[19] D. Mühlbacher, M. Scharber, M. Morana, Z. Zhu, D. Waller, R. Gaudiana, and C. Brabec. High photovoltaic performance of a low-bandgap polymer. *Adv. Mater.*, 18(21):2884–2889, 2006.

[20] Paul F. Barbara, Thomas J. Meyer, and Mark A. Ratner. Contemporary issues in electron transfer research. *J. Phys. Chem.*, 100:13148–13168, 1996.

[21] Peter J. Rossky and John D. Simon. Dynamics of chemical processes in polar solvents. *Nature*, 370:263–269, 1994.

[22] Joachim Stöhr. *NEXAFS Spectroscopy*. Springer-Verlag, Berlin, 1992.

[23] P. A. Bruhwiler, O. Karis, and N. Martensson. Charge-Transfer Dynamics Studied Using Resonant Core Spectroscopies. *Rev. Mod. Phys.*, 74:703–740, 2002.

[24] J. Peet, J. Y. Kim, N. E. Coates, W. L. Ma, D. Moses, A. J. Heeger, and G. C. Bazan. Efficiency Enhancement in Low-Bandgap Polymer Solar Cells by Processing with Alkane Dithiols. *Nat. Mater.*, 6:497–500, 2007.

[25] S. H. Park, A. Roy, S. Beaupre, S. Cho, N. Coates, J. S. Moon, D. Moses, M. Leclerc, K. Lee, and A. J. Heeger. Natural Transition Orbitals. *Nat. Photonics*, 3:297–U5, 2009.

[26] S. Albrecht, S. Schaefer, I. Lange, S. Yilmaz, I. Dumsch, S. Allard, U. Scherf, A. Hertwig, and D. Neher. Light Management in PCPDTBT:PC70BM Solar Cells: A Comparison of Standard and Inverted Device Structures. *Org. Electron.*, 13:615–622, 2012.

[27] A. D. Becke. Density functional thermochemistry. iii. the role of exact exchange. *J. Chem. Phys.*, 98:5648, 1993.

[28] C. Lee, W. Yang, and R. G. Parr. Development of the colle-salvetti correlation-energy formula into a functional of the electron density. *Phys. Rev. B*, 37:785, 1988.

[29] P. J. Stephens, F. J. Devlin, C. F. Chabalowski, and M. J. Frisch. Ab initio calculation of vibrational absorption and circular dichroism spectra using density functional force fields. *J. Phys. Chem.*, 98(45):11623–11627, 1994.

[30] M. J. Frisch, G. W. Trucks, H. B. Schlegel, G. E. Scuseria, M. A. Robb, J. R. Cheeseman, G. Scalmani, V. Barone, B. Mennucci, G. A. Petersson, H. Nakatsuji, M. Caricato, X. Li, H. P. Hratchian, A. F. Izmaylov, J. Bloino, G. Zheng, J. L. Sonnenberg, W. Liang, M. Hada, M. Ehara, K. Toyota, R. Fukuda, J. Hasegawa, M. Ishida, T. Nakajima, Y. Honda, O. Kitao, H. Nakai, T. Vreven, Jr. J. A. Montgomery, J. E. Peralta, F. Ogliaro, M. Bearpark, J. J. Heyd, E. Brothers, K. N. Kudin, V. N. Staroverov, T. Keith, R. Kobayashi, J. Normand, K. Raghavachari, A. Rendell, J. C. Burant, S. S. Iyengar, J. Tomasi, M. Cossi, N. Rega, J. M. Millam, M. Klene, J. E. Knox, J. B. Cross, V. Bakken, C. Adamo, J. Jaramillo, R. Gomperts, R. E. Stratmann, O. Yazyev, A. J. Austin, R. Cammi, C. Pomelli, J. W. Ochterski, R. L. Martin, K. Morokuma, V. G. Zakrzewski, G. A. Voth, P. Salvador, J. J. Dannenberg, S. Dapprich, P. V. Parandekar, N. J. Mayhall, A. D. Daniels, Ö. Farkas, J. B. Foresman, J. V. Ortiz, J. Cioslowski, and D. J. Fox. Gaussian Development Version Revision H.12+. Gaussian Inc., Wallingford CT 2011.

[31] Wenkel Liang, Sean A. Fischer, Michael J. Frisch, and Xiaosong Li. Energy-specific linear response tdhf/tddft for calculating high-energy excited states. *J. Chem. Theor. Comput.*, 7(11):3540–3547, 2011.

[32] R. L. Martin. Natural Transition Orbitals. *J. Chem. Phys.*, 118:4775–4777, 2003.

[33] R. W. Schoenlein, S. Chattopadhyay, H. H. W. Chong, T. E. Glover, P. A. Heimann, C. V. Shank, A. A. Zholents, and M. S. Zolotorev. Generation of femtosecond pulses of synchrotron radiation. *Science*, 287(5461):2237–2240, 2000.

[34] Ivan V. Tomov, Dmitri A. Oulianov, Peilin Chen, , and Peter M. Rentzepis. Ultrafast time-resolved transient structures of solids and liquids studied by means of x-ray diffraction and exafs. *J. Phys. Chem. B*, 103(34):7081–7091, 1999.

[35] Christoph Rose-Petruck, Ralph Jimenez, Ting Guo, Andrea Cavalleri, Craig W Siders, Ferenc Rksi, Jeff A Squier, Barry C Walker, Kent R Wilson, and Christopher P J Barty. Picosecond–milliångström lattice dynamics measured by ultrafast X-ray diffraction. *Nature*, 398(6725):310–312, 1999.

[36] C Rischel, A Rousse, I Uschmann, P A Albouy, J P Geindre, P Audebert, J C Gauthier, E Forster, J L Martin, and A Antonetti. Femtosecond time-resolved X-ray diffraction from laser-heated organic films. *Nature*, 390(6659):490–492, 1997.

[37] R. Krishnan, J. S. Binkley, R. Seeger, and J. A. Pople. Self-consistent molecular orbital methods. xx. a basis set for correlated wave functions. *J. Chem. Phys.*, 72(1), 1980.

[38] Timothy Clark, Jayaraman Chandrasekhar, Günther W. Spitznagel, and Paul Von Ragué Schleyer. Efficient diffuse function-augmented basis sets for anion calculations. iii. the 3-21+G basis set for first-row elements, li–f. *J. Comput. Chem.*, 4(3):294–301, 1983.

[39] Florian Weigend and Reinhart Ahlrichs. Balanced basis sets of split valence, triple zeta valence and quadruple zeta valence quality for h to rn: Design and assessment of accuracy. *Phys. Chem. Chem. Phys.*, 7:3297–3305, 2005.

[40] Dmitrij Rappoport and Filipp Furche. Property-optimized gaussian basis sets for molecular response calculations. *J. Chem. Phys.*, 133(13), 2010.

[41] David Feller. The role of databases in support of computational chemistry calculations. *J. Comput. Chem.*, 17(13):1571–1586, 1996.

[42] Karen L. Schuchardt, Brett T. Didier, Todd Elsethagen, Lisong Sun, Vidhya Gurumoorthi, Jared Chase, Jun Li, , and Theresa L. Windus. Basis set exchange: A community database for computational sciences. 47(3):1045–1052, 2007. PMID: 17428029.

[43] Thom H. Dunning. Gaussian basis sets for use in correlated molecular calculations. i. the atoms boron through neon and hydrogen. *J. Chem. Phys.*, 90(2), 1989.

[44] Rick A. Kendall, Thom H. Dunning, and Robert J. Harrison. Electron affinities of the first-row atoms revisited. systematic basis sets and wave functions. *J. Chem. Phys.*, 96(9), 1992.

[45] David E. Woon and Thom H. Dunning. Gaussian basis sets for use in correlated molecular calculations. iv. calculation of static electrical response properties. *J. Chem. Phys.*, 100(4), 1994.

[46] David E. Woon and Thom H. Dunning. Gaussian basis sets for use in correlated molecular calculations. v. core-valence basis sets for boron through neon. *J. Chem. Phys.*, 103(11), 1995.

[47] Axel D. Becke. A new mixing of hartree–fock and local density-functional theories. *J. Chem. Phys.*, 98(2), 1993.

[48] Axel D. Becke. Density-functional thermochemistry. iii. the role of exact exchange. *J. Chem. Phys.*, 98(7), 1993.

[49] P. J. Stephens, F. J. Devlin, C. F. Chabalowski, and M. J. Frisch. Ab initio calculation of vibrational absorption and circular dichroism spectra using density functional force fields. *J. Phys. Chem.*, 98(45):11623–11627, 1994.

[50] Carlo Adamo and Vincenzo Barone. Toward reliable density functional methods without adjustable parameters: The PBE0 model. *J. Chem. Phys.*, 110(13), 1999.

[51] John P. Perdew, Kieron Burke, and Matthias Ernzerhof. Generalized gradient approximation made simple. *Phys. Rev. Lett.*, 77:3865–3868, Oct 1996.

[52] A. D. Becke. Density functional calculations of molecular bond energies. *J. Chem. Phys.*, 84(8), 1986.

[53] John P. Perdew. Density-functional approximation for the correlation energy of the inhomogeneous electron gas. *Phys. Rev. B*, 33:8822–8824, Jun 1986.

[54] Jochen Heyd and Gustavo E. Scuseria. Efficient hybrid density functional calculations in solids: Assessment of the heyd–scuseria–ernzerhof screened coulomb hybrid functional. *J. Chem. Phys.*, 121(3), 2004.

[55] Jochen Heyd and Gustavo E. Scuseria. Assessment and validation of a screened coulomb hybrid density functional. *J. Chem. Phys.*, 120(16), 2004.

[56] Aliaksandr V. Krukau, Oleg A. Vydrov, Artur F. Izmaylov, and Gustavo E. Scuseria. Influence of the exchange screening parameter on the performance of screened hybrid functionals. *J. Chem. Phys.*, 125(22), 2006.

[57] Oleg A. Vydrov and Gustavo E. Scuseria. Assessment of a long-range corrected hybrid functional. *J. Chem. Phys.*, 125(23), 2006.

[58] Serena DeBeer George, Taras Petrenko, and Frank Neese. Prediction of iron k-edge absorption spectra using time-dependent density functional theory. *J. Phys. Chem. A*, 112(50):12936–12943, 2008. PMID: 18698746.

[59] Nicholas A. Besley and Frans A. Asmuruf. Time-dependent density functional theory calculations of the spectroscopy of core electrons. *Phys. Chem. Chem. Phys.*, 12:12024–12039, 2010.

[60] G. Fronzoni, R. De Francesco, , and M. Stener. Time dependent density functional theory of x-ray absorption spectroscopy of alkaline-earth oxides. *J. Phys. Chem. B*, 109(20):10332–10340, 2005. PMID: 16852252.

[61] Serena DeBeer George, Taras Petrenko, and Frank Neese. Time-dependent density functional calculations of ligand k-edge x-ray absorption spectra. *Inorganica Chimica Acta*, 361(4):965 – 972, 2008. Protagonists in Chemistry: Professor Edward I Solomon.

[62] M. J. Frisch, G. W. Trucks, H. B. Schlegel, G. E. Scuseria, M. A. Robb, J. R. Cheeseman, G. Scalmani, V. Barone, B. Mennucci, G. A. Petersson, H. Nakatsuji, M. Caricato, X. Li, H. P. Hratchian, A. F. Izmaylov, J. Bloino, G. Zheng, J. L. Sonnenberg, W. Liang, M. Hada, M. Ehara, K. Toyota, R. Fukuda, J. Hasegawa, M. Ishida, T. Nakajima, Y. Honda, O. Kitao, H. Nakai, T. Vreven, J. A. Montgomery Jr., J. E. Peralta, F. Ogliaro, M. Bearpark, J. J. Heyd, E. Brothers, K. N. Kudin, V. N. Staroverov, T. Keith, R. Kobayashi, J. Normand, K. Raghavachari, A. Rendell, J. C. Burant, S. S. Iyengar, J. Tomasi, M. Cossi, N. Rega, J. M. Millam, M. Klene, J. E. Knox, J. B. Cross, V. Bakken, C. Adamo, J. Jaramillo, R. Gomperts, R. E. Stratmann, O. Yazyev, A. J. Austin, R. Cammi, C. Pomelli, J. W. Ochterski, R. L. Martin, K. Morokuma, V. G. Zakrzewski, G. A. Voth, P. Salvador, J. J. Dannenberg, S. Dapprich, P. V. Parandekar, N. J. Mayhall, A. D. Daniels, Ö. Farkas, J. B. Foresman, J. V. Ortiz, J. Cioslowski, and D. J. Fox. Gaussian Development Version Revision H.13. Gaussian Inc., Wallingford CT 2012.

[63] M. Domke, C. Xue, A. Puschmann, T. Mandel, E. Hudson, D.A. Shirley, and G. Kaindl. Carbon and oxygen k-edge photoionization of the co molecule. *Chem. Phys. Lett.*, 173(1):122 – 128, 1990.

[64] G. Remmers, M. Domke, A. Puschmann, T. Mandel, C. Xue, G. Kaindl, E. Hudson, and D. A. Shirley. High-resolution *K*-shell photoabsorption in formaldehyde. *Phys. Rev. A*, 46:3935–3944, Oct 1992.

[65] M Tronc, G C King, and F H Read. Carbon *K*-shell excitation in small molecules by high-resolution electron impact. *J. Phys. B*, 12(1):137, 1979.

[66] E. Shigemasa, K. Ueda, Y. Sato, T. Sasaki, and A. Yagishita. Symmetry-resolved *K*-shell photoabsorption spectra of free n_2 molecules. *Phys. Rev. A*, 45:2915–2921, Mar 1992.

[67] J. Schirmer, A. B. Trofimov, K. J. Randall, J. Feldhaus, A. M. Bradshaw, Y. Ma, C. T. Chen, and F. Sette. *K*-shell excitation of the water, ammonia, and methane molecules using high-resolution photoabsorption spectroscopy. *Phys. Rev. A*, 47:1136–1147, Feb 1993.

[68] Jun-ichi Adachi, Nobuhiro Kosugi, Eiji Shigemasa, and Akira Yagishita. Renner–teller effect and rydberg-valence mixing in the n and o k-edge photoabsorption spectra of n_2o. *J. Chem. Phys.*, 102(19), 1995.

[69] R. Püttner, I. Dominguez, T. J. Morgan, C. Cisneros, R. F. Fink, E. Rotenberg, T. Warwick, M. Domke, G. Kaindl, and A. S. Schlachter. Vibrationally resolved o 1*s* core-excitation spectra of co and no. *Phys. Rev. A*, 59:3415–3423, May 1999.

[70] K. Lopata, B. E. Van Kuiken, M. Khalil, and N. Govind. Linear-response and real-time time-dependent density functional theory studies of core-level near-edge x-ray absorption. *J. Chem. Theor. Comput.*, 8(9):3284–3292, 2012. PMID: 26605735.

[71] Jong-Won Song, Mark A. Watson, Ayako Nakata, and Kimihiko Hirao. Core-excitation energy calculations with a long-range corrected hybrid exchange-correlation functional including a short-range gaussian attenuation (lcgau-bop). *J. Chem. Phys.*, 129(18), 2008.

[72] Nicholas A. Besley, Michael J. G. Peach, and David J. Tozer. Time-dependent density functional theory calculations of near-edge x-ray absorption fine structure with short-range corrected functionals. *Phys. Chem. Chem. Phys.*, 11:10350–10358, 2009.

[73] Shashi P Karna, Paras N Prasad, and Michel Dupuis. Nonlinear Optical Properties of p-Nitroaniline: an ab Initio Time-DDependentependent Coupled Perturbed Hartree-Fock Study. *J. Chem. Phys.*, 94(2):1171, 1991.

[74] Kurt V Mikkelsen, Yi Luo, Hans Ågren, and Poul Jørgensen. Solvent Induced Polarizabilities and Hyperpolarizabilities of Para-nitroaniline Studied by Reaction Field Linear Response Theory. *J. Chem. Phys.*, 100(11):8240, 1994.

[75] Vadim M Farztdinov, Roland Schanz, Sergey A Kovalenko, and Nikolaus P Ernsting. Relaxation of Optically Excited p-Nitroaniline: Semiempirical Quantum-Chemical Calculations Compared to Femtosecond Experimental Results. *J. Phys. Chem. A*, 104(49):11486–11496, dec 2000.

[76] E R Davidson, B E Eichinger, and B H Robinson. Hyperpolarizability: Calibration of Theoretical Methods for Chloroform, Water, Acetonitrile, and p-Nitroaniline. *Opt. Mater.*, 29(4):360–364, dec 2006.

[77] BF Levine. Donor-Acceptor Charge Transfer Contributions to the Second Order Hyperpolarizability. *Chem. Phys. Lett.*, 37(3):516–520, 1976.

[78] Wouter Schuddeboom, John M. Warman, H. A. M. Biemans, and E. W. Meijer. Dipolar triplet states of p-nitroaniline and n-alkyl derivatives with one-, two-, and three-fold symmetry. *J. Phys. Chem.*, 100(30):12369–12373, 1996.

[79] CL Thomsen, J. Thøgersen, and SR Keiding. Ultrafast Charge-Transfer Dynamics: Studies of p-Nitroaniline in Water and Dioxane. *J. Phys. Chem. A*, 102(7):1062–1067, 1998.

[80] R. Wortmann, P. Kramer, C. Glania, S. Lebus, and N. Detzer. Deviations from Kleinman Symmetry of the Second-order Polarizability Tensor in Molecules with Low-lying Perpendicular Electronic Bands. *Chem. Phys.*, 173(1):99–108, 1993.

[81] N. Ghoneim and P. Suppan. Solvatochromic shifts of non-dipolar molecules in polar solvents. *Spectrochim. Acta A*, 51(6):1043 – 1050, 1995.

[82] H. J. Freund R. Bigelow and B. Dick. The t1 state of p-nitroaniline and related molecules: a cndo/s study. *Theor. Chem. Acc.*, 63, 1986.

[83] Wenkel Liang, Craig T. Chapman, Feizhi Ding, and Xiaosong Li. Modeling ultrafast solvated electronic dynamics using time-dependent density functional theory and polarizable continuum model. *J. Phys. Chem. A*, 116(8):1884–1890, 2012.

[84] Jacopo Tomasi and Maurizio Persico. Molecular interactions in solution: An overview of methods based on continuous distributions of the solvent. *Chem. Rev.*, 94:2027–2094, 1994.

[85] Thanh N. Truong. Quantum modelling of reactions in solution: an overview of dielectric continuum methodology. *Int. Rev. Phys. Chem.*, 17 (4):525–546, 1998.

[86] W. Hackbusch. *Integral Equations: Theory and Numerical Treatment*. Birkhäuser Verlag, Basel, Switzerland, 1995.

[87] Benedetta Mennucci, E Cancès, and Jacopo Tomasi. Evaluation of Solvent Effects in Isotropic and Anisotropic Dielectrics and in Ionic Solutions with a Unified Integral Equation Method: Theoretical Bases, Computational Implementation, and Numerical Applications. *J. Phys. Chem. B*, 101(49):10506–10517, 1997.

[88] E Cancès, Benedetta Mennucci, and Jacopo Tomasi. A New Integral Equation Formalism for the Polarizable Continuum Model: Theoretical Background and Applications to Isotropic and Anisotropic Dielectrics. *J. Chem. Phys.*, 107(8):3032, 1997.

[89] E Cancès and Benedetta Mennucci. New Applications of Integral Equations Methods for Solvation Continuum Models: Ionic Solutions and Liquid Crystals. *J. Math. Phys.*, 23(3):309–326, 1998.

[90] Giovanni Scalmani and Michael J. Frisch. Continuous surface charge polarizable continuum models of solvation. i. general formalism. *J. Chem. Phys.*, 132:114110, 2000.

[91] Marco Caricato, Francesca Ingrosso, Benedetta Mennucci, and Jacopo Tomasi. A Time-Dependent Polarizable Continuum Model: Theory and Application. *J. Chem. Phys.*, 122(15):154501, 2005.

[92] Benedetta Mennucci, J. Tomasi, R Cammi, J R Cheeseman, M J Frisch, F J Devlin, S Gabriel, and P J Stephens. Polarizable Continuum Model (PCM) Calculations of Solvent Effects on Optical Rotations of Chiral Molecules. *J. Phys. Chem. A*, 106(25):6102–6113, jun 2002.

[93] Francesca Ingrosso, Benedetta Mennucci, and Jacopo Tomasi. Quantum Mechanical Calculations Coupled with a Dynamical Continuum Model for the Description of Dielectric Relaxation: Time Dependent Stokes Shift of Coumarin C153 in Polar Solvents. *J. Mol. Liq.*, 108(1-3):21–46, November 2003.

[94] Marco Caricato, Benedetta Mennucci, Jacopo Tomasi, Francesca Ingrosso, Roberto Cammi, Stefano Corni, and Giovanni Scalmani. Formation and Relaxation of Excited States in Solution: a New Time Dependent Polarizable Continuum Model Based on Time Dependent Density Functional Theory. *J. Chem. Phys.*, 124(12):124520, 2006.

[95] Benedetta Mennucci. Time Dependent Solvation: a New Frontier for Quantum Mechanical Continuum Models. *Theor. Chem. Acc.*, 116(1-3):31–42, October 2006.

[96] Roberto Cammi, Benedetta Mennucci, and Jacopo Tomasi. Fast evaluation of geometries and properties of excited molecules in solution: A tamm-dancoff model with application to 4-dimethylaminobenzonitrile. *J. Phys. Chem.*, 104:5631, 2000.

[97] Giovanni Scalmani, Michael J Frisch, Benedetta Mennucci, Jacopo Tomasi, Roberto Cammi, and Vincenzo Barone. Geometries and Properties of Excited States in the Gas Phase and in Solution: Theory and Application of a Time-Dependent Density Functional Theory Polarizable Continuum Model. *J. Chem. Phys.*, 124(9):094107, 2006.

[98] B. Bagchi, D.W. Oxtoby, and G.R. Fleming. Theory of the Time Development of the Stokes Shift in Polar Media. *Chem. Phys.*, 86(3):257–267, 1984.

[99] Vincenzo Barone, Michael J Frisch, Giovanni Scalmani, Konstantin N Kudin, Gustavo E Scuseria, and Christian S Pomelli. Achieving Linear-Scaling Computational Cost for the Polarizable Continuum Model Of Solvation. *Theor. Chem. Acc.*, 111(2-6):90–100, March 2004.

[100] Michael A Kahlow, Wlodzimierz Jarzeba, Tai Jong Kang, and Paul F. Barbara. Femtosecond Resolved Solvation Dynamics in Polar Solvents. *J. Chem. Phys.*, 90(1):151, 1989.

[101] V. Barone, M. Cossi, and Jacopo Tomasi. Geometry Optimization of Molecular Structures in Solution by the Polarizable Continuum Model. *J. Comput. Chem.*, 19(4):404–417, 1998.

[102] SA Kovalenko, R. Schanz, VM Farztdinov, H. Hennig, and NP Ernsting. Femtosecond Relaxation of Photoexcited para-Nitroaniline: Solvation, Charge Transfer, Internal Conversion and Cooling. *Chem. Phys. Lett.*, 323(3):312–322, 2000.

[103] M. E. Casida. Time-dependent density-functional response theory for molecules. In D.P. Chong, editor, *Recent Advances in Density Functional Methods, Part I*, page 155. World Scientific, 1995.

[104] Mark E Casida, Christine Jamorski, Kim C Casida, and Dennis R Salahub. Molecular excitation energies to high-lying bound states from time-dependent density-functional response theory: Characterization and correction of the time-dependent local density approximation ionization threshold. *J. Chem. Phys.*, 108(11):4439, 1998.

[105] Gustavo E Scuseria. Linear Scaling Density Functional Calculations with Gaussian Orbitals. *J. Phys. Chem. A*, 103(25):4782–4790, June 1999.

[106] Andreas Dreuw and Martin Head-Gordon. Single-Reference ab Initio Methods for the Calculation of Excited States of Large Molecules. *Chem. Rev.*, 105(11):4009–4037, nov 2005.

[107] D. Kosenkov and L. V. Slipchenko. Solvent effects on the electronic transitions of p-nitroaniline: A QM/EFP study. *J. Phys. Chem. A*, 115:392–401, 2011.

[108] A.M. Moran, A. Myers Kelley, and S. Tretiak. Excited State Molecular Dynamics Simulations of Nonlinear Push–Pull Chromophores. *Chem. Phys. Lett.*, 367(3):293–307, 2003.

[109] Filippo Lipparini, Giovanni Scalmani, Benedetta Mennucci, Eric Cancès, Marco Caricato, and Michael J Frisch. A Variational Formulation of the Polarizable Continuum Model. *J. Chem. Phys.*, 133(1):014106, 2010.